

# Effect of flange waviness on the C1 Wedge Connection

**Master's Thesis**

George Misios

Faculty of Civil Engineering and  
Geosciences

Delft University of Technology

June 2019, Delft





# Effect of flange waviness on the C1 Wedge Connection

By  
George Misios

in partial fulfilment of the requirements for the degree of

**Master of Science**  
in Civil Engineering

at the Delft University of Technology,  
to be defended publicly on Monday 3 of June 2019.

Student number:	4631714	
Thesis committee:	Prof.Dr.M. Veljkovic,	TU Delft-Chairman
	Dr.ir. M.A.N. Hendriks,	TU Delft
	Dr. Haohui Xin,	TU Delft
	Ir.J.S. Winkes,	C1-connections BV
	Ir.K.E.Y. Creusen,	C1-connections BV

*This thesis is confidential and cannot be made public until 03/06/2024.*

An extract electronic version of this thesis is available at <http://repository.tudelft.nl/>.



# Preface

This thesis is made as a completion of my master's degree in Structural Engineering at the faculty of Civil Engineering and Geosciences at Delft University of Technology, the Netherlands.

I would like to express my gratitude to all the individuals that have helped me throughout the compilation of this thesis.

First, I would like to thank my supervisors from the company, Jasper Winkes and Koen Creusen, for proposing such an interesting and challenging topic and their continuously support and guidance during this thesis project.

Also, I would like to thank my university supervisors, Prof.Dr.M. Veljkovic, Dr.ir. M.A.N. Hendriks and Dr.H. Xin for their critical feedback and guidance along the way.

Finally, the unconditional support of my family and my friends, both from Greece and Netherlands, was crucial through the conduction of this thesis, from the beginning to end, and I would like to express my sincere gratitude for everything they offered.

*Georgios Misios  
Delft, June 2019*



# Abstract

Wind turbines constitute a sustainable and effective solution to produce energy using wind power. Offshore wind turbines are becoming of special interest and more demanding with continuously increased diameters. However, their design poses great challenges, since the installation and fabrication tolerances in combination with high cyclic loading play an important role on the fatigue assessment of the wind turbine structure.

One part of specific interest for the fatigue assessment of a wind turbine is the way that the transition piece is connected to monopile. Since now, grouted and bolted connections are commonly used, but they have many drawbacks. These disadvantages regarding their performance inspired by C1 Connections BV to invent a new type of connection to connect large diameter tubulars, the C1 Wedge Connection. This innovation allows to increase the fatigue life of the wind turbine structures and decrease simultaneously their construction and installation cost.

The work that will be presented here deals with the fatigue assessment of the C1 Wedge Connection, and how the presence of imperfections may affect the fatigue life of it.

After analysis of the load path and the innovative preload mechanism, a reference wind turbine has been selected and the 3D CAD software of Solid Edge is used to design all the components of the wedge connection and assemble them to their final position. The stiffness of the main components of the wedge connection (TP-flange, TP-shell and MP) is calculated analytically, based on the method proposed by Seidel and adapted for the C1 Wedge Connection. An analytical model using Timoshenko beam theory has been developed for TP-flange stiffness calculation. This model and all analytical calculations were verified against FEM results built on ANSYS Workbench and mechanical for that purpose.

Once the components' stiffnesses have been calculated based on analytical formulas, an approximation of the maximum closeable gap is plotted for different gap sizes for this specific geometry of the connection and friction coefficient  $\mu=x$  which was proved being conservative after calibration using results from tests taken place at TU Delft lab.

Secondly different scenarios have been investigated using FE models regarding the position of the gap among the different components of the connection. From this analysis, in terms of magnitude of the remaining gap and the reaction force at the interface of both flanges, was concluded that the worst scenario is the presence of imperfection only at MP side.

This worst scenario (only imperfect MP flange) is selected and examined for compression to tension under ULS overturning moment. The fatigue damage of the imperfect structure is calculated and compared with a perfect one. For the purpose of this thesis, preloading has been applied by once at all connections of the ring. Peak stresses are calculated and based on selected S-N curve from DNV-GL codes and by making use of the Miner's rule, the fatigue damage at the critical positions of both perfect and imperfect connection is calculated. For the same imperfect structure, the fatigue damage is calculated again based on nominal stresses measured underneath each hole of imperfect MP segment. In that case the specific for the C1 Wedge Connection S-N curve is used, based on fatigue single segment test results taken place at TU Delft lab, in 2018.

From this research, it is concluded that based on peak stress method the selected imperfect structure is not able to withstand the fatigue damage loads. On the other hand, the same cannot be stated using nominal stress method which is more realistic based on test results and not sensitive to mesh details. In that case the fatigue damage for every hole is  $\ll 1$ .



# Contents

List of Figures .....	9
List of Tables .....	13
<b>1 Introduction .....</b>	<b>1</b>
<b>1.1 Background .....</b>	<b>1</b>
<b>1.2 The concept of the C1 Wedge Connection .....</b>	<b>2</b>
1.2.1 Nomenclature and functional description.....	2
1.2.2 Installation sequence .....	3
<b>1.3 Causes of presence of flange flatness deviations .....</b>	<b>3</b>
<b>1.4 Research questions.....</b>	<b>4</b>
<b>1.5 Methodology of the research.....</b>	<b>5</b>
<b>1.6 Reference geometry .....</b>	<b>6</b>
<b>2 State of the art .....</b>	<b>7</b>
<b>2.1 Description of method proposed by M. Seidel (2018) .....</b>	<b>7</b>
2.1.1 FE-model description for calculation of shell stiffness .....	7
2.1.2 Results.....	8
<b>3 Preload mechanism .....</b>	<b>11</b>
<b>3.1 Load path without preload .....</b>	<b>11</b>
<b>3.2 Load path with preload .....</b>	<b>11</b>
<b>3.3 Spring system stiffness .....</b>	<b>14</b>
3.3.1 Stiffness of the top of lower flange (MP stiffness).....	14
3.3.2 Stiffness of upper flange-fastener assembly (Fastener stiffness).....	14
3.3.3 Overview of results.....	15
<b>3.4 Calculation of required preload .....</b>	<b>16</b>
3.4.1 Segment loads .....	16
3.4.2 Material properties .....	16
3.4.3 Actuation loads .....	17
3.4.4 Self- locking mechanism .....	18
<b>4 Stiffness approximation of the different parts on the C1 Wedge Connection.....</b>	<b>19</b>
<b>4.1 Stiffness estimation of individual components of Upper flange TP.....</b>	<b>19</b>
4.1.1 Stiffness calculation of TP shell using FE analysis .....	19
4.1.2 Analytical estimation of upper flange shell stiffness.....	22
4.1.3 Comparison of analytical and numerical stiffness of TP shell .....	23
4.1.4 Stiffness estimation of TP flange .....	23
4.1.5 FE Models description for calculation of TP flange stiffness .....	25

4.1.6 Comparison of analytical and numerical extracted deflection of TP flange for all three approaches .....	27
4.1.7 Analytical estimation of TP flange stiffness.....	27
4.1.8 Comparison of linear stiffness of TP flange estimated analytically vs numerical results .....	28
<b>4.2 Stiffness estimation of combined Upper flange (TP) .....</b>	<b>29</b>
4.2.1 FE model description for the combined TP stiffness verification .....	30
4.2.2 Magnitude of stresses on TP shell .....	31
4.2.3 Conclusions for combined TP stiffness approximation.....	32
<b>4.3 Stiffness of Lower flange (MP).....</b>	<b>33</b>
4.3.1 Model description for calculation of MP stiffness .....	33
4.3.2 Stiffness calculation of MP stiffness using FE analysis.....	33
4.3.3 Analytical estimation of MP stiffness .....	34
4.3.4 Conclusions for MP stiffness .....	35
<b>4.4 Maximum closeable gap based on component stiffness.....</b>	<b>35</b>
4.4.1 Analytical calculations adapted for the certain case of 15 degrees imperfect segment .....	36
<b>4.5 Conclusions .....</b>	<b>36</b>
<b>5 Behaviour of imperfect structure .....</b>	<b>39</b>
<b>5.1 FE Analysis single segment- Model description .....</b>	<b>39</b>
5.1.1 Geometry .....	39
5.1.2 Contacts.....	40
5.1.3 Materials .....	40
5.1.4 Boundary conditions.....	40
5.1.5 Loads .....	40
5.1.6 Mesh .....	40
<b>5.2 Maximum reaction force verification.....</b>	<b>41</b>
<b>5.3 FE analysis of imperfect full ring structure - Model description .....</b>	<b>41</b>
5.3.1 Geometry .....	41
5.3.2 Materials .....	42
5.3.3 Contacts.....	43
5.3.4 Mesh .....	43
5.3.5 Boundary conditions.....	43
5.3.6 Loads .....	43
<b>5.4 Results .....</b>	<b>44</b>
5.4.1 FE Analysis of structures with imperfect section 30° and gap height x mm .....	44
5.4.2 FE analysis of structures with imperfect section 15° and gap height 0.5mm.....	46
<b>6 Fatigue calculation of imperfect structure .....</b>	<b>47</b>

<b>6.1 FE modelling - Single segment reference model</b> .....	47
6.1.1 Model setup .....	47
<b>6.2 Perfect structure- FE model description</b> .....	48
6.2.1 Geometry .....	48
6.2.2 Materials .....	48
6.2.3 Contact .....	48
6.2.4 Mesh .....	49
6.2.5 Boundary conditions.....	49
6.2.6 Loads.....	49
6.2.7 Results.....	49
<b>6.3 Imperfect structure</b> .....	50
<b>6.4 Stress Concentration Factor calculation for both perfect and imperfect structure</b> .....	50
<b>6.5 Fatigue damage calculation according to DNVGL-RP-C203 based on peak stress</b> .....	52
<b>6.6 Fatigue assessment of imperfect structure based on nominal stress</b> .....	56
6.6.1 Description of method .....	56
6.6.2 Nominal stress curves extracted from FE analysis .....	56
6.6.3 Nominal stress ratio of imperfect structure .....	57
6.6.4 Fatigue damage calculation .....	58
<b>7 Conclusions &amp; Recommendations</b> .....	59
7.1 Conclusions.....	59
7.2 Recommendations .....	60
7.3 Industry guidelines.....	60
<b>8 Bibliography</b> .....	63
<b>9 Appendix A: Solution of Analytical Timoshenko model using MAPLE software</b> .....	65
9.1 Deriving the governing equations of analytical model .....	65
9.2 Solving the governing differential equations .....	70
<b>10 Appendix B: Input data for ANSYS</b> .....	71
10.1 Steel.....	71
<b>11 Appendix C: Input data for analytical calculations</b> .....	71
11.1 Second moment of Inertia .....	71
11.2 Shear Area $A_{eff}$ .....	72



# List of Figures

Figure 1.3- Flange deviation of flange contact area.....	4
Figure 1.4- Gap at one flange.....	4
Figure 2.1- FE model for determination of upper flange shell stiffness where circle indicates area where the gap is simulated.....	7
Figure 2.2- Stiffness vs gap angle for different combinations. ....	8
Figure 3.2- Parallel spring model.....	11
Figure 3.3- Preloaded lower flange subjected to tension. ....	12
Figure 3.4- Preloaded lower flange subjected to compression. ....	13
Figure 3.7- Load-displacement diagram preloaded connection. ....	15
Figure 3.8- Free body diagram of a single wedge, generating half of the required preload. The red arrows, representing normal force to the inclined planes, are in reality perpendicular to the surface. .	17
Figure 3.9- Relationship between bolt force ( $F_{hor}$ ) and vertical preload ( $F_{preload}$ ) for different friction coefficients. ....	18
Figure 4.1- FE model for determination of TP-shell stiffness. ....	19
Figure 4.2- Fixed boundary conditions in all translational directions along the circumference (a) and free to deform longitudinally at the segment where the gap is present (b). ....	20
Figure 4.3- Uniform distributed load along the whole circumference of TP shell. ....	20
Figure 4.4- Mesh used for this certain group of analysis. ....	21
Figure 4.5- Stiffness of TP-shell vs gap angle for all data points of numerical study. ....	22
Figure 4.6- Comparison of analytically estimated stiffness vs shell stiffness from FE model. ....	23
Figure 4.9- Boundary conditions and position of the load.....	25
Figure 4.10- Position of the extracted deformation along z axes.....	25
Figure 4.12- Position and magnitude of load used at the second step. ....	26
Figure 4.15- Parallel spring model which represents the combined Upper flange (TP). ....	29
Figure 4.22- Stiffness of MP vs gap angle for all data points of numerical study. ....	33
Figure 4.23- Comparison of analytically estimated stiffness vs MP stiffness from FE model. ....	35
Figure 5.9- Preload for lower (left) and Upper flange (right). ....	43
Figure 6.11- Applying preload on both inner and outer wedge at all fastener assemblies around the circumference.....	49
Figure 6.17- Load spectrum used for the fatigue analysis of perfect & imperfect structure with an identical part of the table.....	52
Figure 6.20- Stress range reduction factor to be used with the S-N curve for base material [8]. ....	54
Figure 6.21- S-N curves in air.[8].....	54
Figure 9.1- Overview of analytical model schematization. ....	65
Figure 9.2- Assumed directions for derivation of kinematic equations. ....	66
Figure 9.3- Positive force directions equilibrium equations. ....	67
Figure 9.4- Analytical model with solution field.....	69
Figure 11.1- Cross section of TP flange used for calculation of the second moment of inertia. ....	71



# List of Tables

Table 1- Vertical deformation at the middle of the beam for three different geometries and for three different lengths. ....	27
Table 2- TP flange vs TP shell stiffness comparison based on analytical calculation. ....	29
Table 3- Comparison of linear stiffness of combined TP extracted from FEA vs analytical method for four different gap angles. ....	30
Table 4- Ratio of gap length vs affected TP shell height. ....	31
Table 5- Contact definitions FE model. ....	40
Table 6- Contact definitions FE model. ....	43
Table 7- Magnitude of the gap for all three cases after the end of the two loading steps. ....	44
Table 8- Magnitude of the gap for all cases after the end of the two loading steps. ....	46
Table 9- Contact surface definition FE model. ....	48
Table 11- S-N curves in air.[8] ....	54
Table 12- Fatigue damage for perfect structure. ....	56
Table 13- Fatigue damage for imperfect structure. ....	56
Table 14- Fatigue damage of imperfect structure based on nominal stress. ....	58
Table 15- Fatigue damage for perfect structure based on peak stress. ....	59
Table 16- Fatigue damage for imperfect structure based on peak stress. ....	59
Table 17- Fatigue damage of imperfect MP based on nominal stress. ....	60
Table 18- Overview of boundary conditions analytical model. ....	69
Table 19: Density and Elastic for structural steel. ....	71



# 1 Introduction

## 1.1 Background

Nowadays, the request in sustainable power sources expands to an ever-increasing extent. Along with the growing interest for “green” energy, the wind sector has been developed dramatically the past decades. Both the number of the installed wind turbines and the sizes of them are increasing. Wind turbines constitute the most cost-effective way of the exploitation of the available wind potential; thus, investigation of such structures is of particular interest. They may be constructed either land areas (on-shore) or sea areas (off-shore). Offshore wind turbines are becoming of special interest in recent years. Although an offshore wind turbine usually starts with a higher initial cost, it can outweigh a similar onshore one during its service life in a number of aspects such as: higher productivity due to stronger winds over sea areas, larger available installation areas and lower (or even non-existent) public nuisance [\[10\]](#).

A wind turbine could be considered as a structure that lies between a civil engineering structure and a machine [\[11\]](#). More specifically, a wind turbine consists of structural elements (tower, substructure etc.) and several electrical and machine components with a control system (gear box, drivetrain etc.). Under a civil engineering perspective, the main components of a wind turbine could be considered the tower and the substructure. The tower is the element on the top of which the mechanical parts of the wind turbines, such as the nacelle and the blades are installed. The tower is made of steel, has a circular cross section and is usually tapered (the cross-section size decreases with height linearly). The tower is connected to the substructure, the part of the wind turbine that is submerged in the water. The substructure may be founded directly in the seabed or based on a floating platform. Thus, there are two types of the substructure foundation, namely floating, which is by wires anchored at the bottom of the seabed, and fixed. Fixed wind turbines are used especially in sites of low or medium depths, while the construction of floating wind turbines is cost-effective in case of deep waters. The most common type of design for fixed wind turbines, which is used for depths of approximately 30 meters, is the monopile. The monopile support structure of an offshore wind turbine consists of two parts: the monopile penetrating at seabed and the transition piece connected to the monopile and the tower. The advantages of a monopile support structure, when compared with the other bottom fixed support structures, include minimal seabed preparation requirements, most competitive manufacturing costs owing to the simple structure and the most experienced support structure with offshore wind turbines. The disadvantages include structure flexibility at large water depths, time-consuming installation and manufacturing constraints for large diameters and thickness that makes it difficult to go beyond 50m water depth.

Regardless of the type of an offshore wind turbine, both structure and substructure are subjected to cyclic loads with a wide range of frequencies. This fact may arise critical issues during the turbine’s service life in terms of fatigue and power efficiency. Hence fatigue becomes potentially one of the main problems causing degradation in the long-term structural integrity. An item closely related to that, is both monopile and transition piece due to fabrication and installation tolerances are not always perfectly aligned, producing gaps at their contact surface. This can reduce even more the fatigue life of the structure.

Special focus should be devoted to the appropriate design and analysis of this kind of structures for a safer and more reliable operation. Because a turbine system's cost is determined by its target reliability, it is important to achieve a trade-off among the failure consequences, material consumption and failure probability at the design stage [11].

One part of specific interest for the fatigue assessment of a wind turbine is the way that the transition piece is connected to the monopile. A novel connection method for offshore wind foundations has been invented by C1 Connections B.V. The main goal was to create a new type of connection that is economic, safe, fast reliable and fail safe compared to the conventional bolted / grouted connections that are used until now.

## 1.2 The concept of the C1 Wedge Connection

The C1 Wedge Connection is a new concept developed by **C1 Connections B.V** to connect large diameter tubulars, such as a monopile (MP) and a transition piece (TP) (**Error! Reference source not found.**). Many holes and fasteners are distributed around the circumference of the tubulars. The fastener assembly consists of 2 blocks and two wedges and a bolt, which creates a vertically expanding mechanism. This fastener is applied through over-dimensioned holes in the TP and MP. Due to the certain geometry of the connection, before applying preload, the fastener assembly is in contact at the top with the MP and at the lowest part with the TP (**Error! Reference source not found.**). After the application of preload, the wedges are pulled together with a bolt. The horizontal movement expands the blocks vertically, which in turn compresses the MP and TP together. The bolt force is magnified into a vertical preload through the inclined planes.

### 1.2.1 Nomenclature and functional description

The Wedge Connection is a flanged fork-eye connection between two tubular members of an offshore wind turbine. The upper flange is welded to upper tubular section, the lower flange may be an integral component of the lower tubular. The fastener is the connecting element between the two flanges. A few fastener assemblies are evenly distributed over the circumference of the section. These fastener assemblies consist of five main components namely: an upper and lower block, two wedges in between the blocks, and a bolt which is connects the wedges.

#### Lower flange

The lower flange is fitted to the lower tubular member. It can either be a separate flange, or it can be an integral component of the tubular. The steel flange has elongated holes with the top and bottom with constant radius. The upper block is in contact with the lower flange through the top of this hole.

#### Upper flange

The upper flange is fitted to the upper tubular member. It is a solid (forged) flange. The main feature of the flange are the two webs. The webs contain elongated holes with a top and

bottom with constant radius. The lower block is in contact with the upper flange through the lower radius of the hole.

### **Fastener assembly**

The fastener assembly consists of five components: the upper and lower block, the inner and the outer wedge and the bolt. The fastener connects the upper and the lower flange by expanding vertically. This is achieved by the inclined plane between the blocks and the wedges.

### **Blocks**

The blocks span the full width of the TP flange. The lower shell is in contact with the TP flange, while the upper block is in contact with the lower flange (MP). These contact areas are rounded with a constant radius. The width of the fastener assembly is just under twice the radius, so there is some room for movement. The other side of the shells are fitted with inclined planes. A constant plane is defined by changing the angle of the inclined plane along the length of the blocks.

### **Wedges**

The wedges connect the upper and lower block through the inclined planes. The outer wedge is fitted with a blind threaded hole, while the inner wedge is fitted with a hole through which the bolt moves. By turning the bolt, the wedges are pulled together.

### **Bolt**

The bolt is used to pull the wedges together, which expands the blocks and therefore fixed the connection. Applying further torque to the bolt creates additional horizontal load on the wedges, which result in preload in the contact plane between MP and TP. The bolt is only threaded at the end which is inserted in the outer wedge. This ensures the bolt shaft is smooth in the center of the span, preventing crack initiation. The head of the bolt is fitted with a HYTORC Washer. This simple system ensures the reaction load of the installation tool is supplied internally. No separate reaction arm is required.

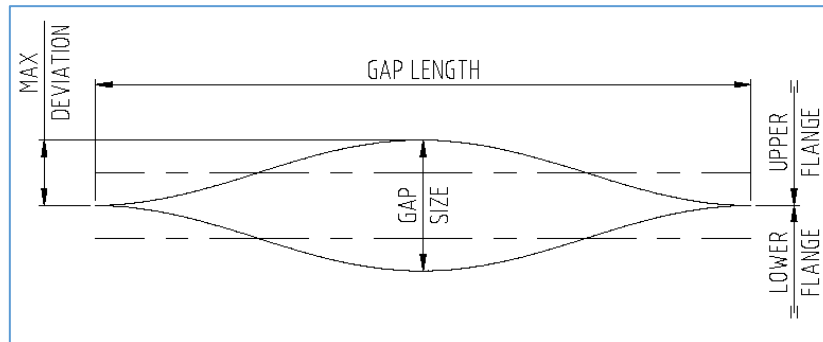
## **1.2.2 Installation sequence**

1. The pile that is welded to lower flange is driven into the seabed by a piling hammer
2. The upper tubular, containing the fasteners, is installed on the top of the lower flange and the holes are aligned
3. The fasteners are displaced radially outward
4. Torque is applied to the bolt, pulling the wedges together
5. The horizontal actuation force on the wedges is converted into a vertical preload through the inclined planes of wedge and upper and lower block
6. The vertical preload induces a contact load between both flanges

## **1.3 Causes of presence of flange flatness deviations**

The upper flange is connected to the tubular sections by welding, while the lower flange can be made by directly machining the upper section of the MP. The uneven weld shrinkage will

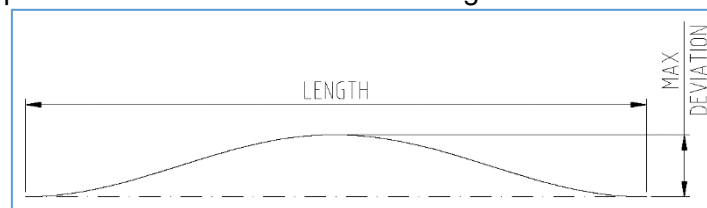
result in flatness deviations in the contact areas of both flanges, leading to local gap in the contact plane after installation. Characteristics in order to define the size of the gap and nomenclature are presented in the following figures.(Figure 1.3, Figure 1.4)



The local gap between two flanges is quantified with two variables:

- Gap length (expressed in meters or as a sector angle of the tubular section)
- Gap size (the opening flanges)

At this point must the shape of the having a perfect with the ends tangential to the horizontal plane.



maximum between both be referred that gap was selected sinusoidal shape

## 1.4 Research questions

The main aim of this thesis is to investigate the behaviour of an imperfect wind turbine structure where the C1 Wedge Connection is used for TP/MP connection. The following research questions will be answered in this thesis:

- What is the behaviour of the components of the connection in terms of stiffness?
- How is the largest gap that can be closed from this connection given a certain gap length according to analytical calculations?
- How is the response of an imperfect structure exposed to external load in terms of magnitude of the gap and reaction force at the MP/TP interface?
- How is the fatigue damage of an imperfect structure compared to a perfect one based on peak stress and nominal stress method?

## 1.5 Methodology of the research

As the C1 Wedge Connection is a new innovative connection, literature study is performed to the preload mechanism of a perfect connection. As closely related to the behaviour of an imperfect structure is the stiffness of different components of the connection, literature study has been performed on stiffness approximation of the different parts on L-flange bolted connection.

Based on this method, at the first step the C1 Wedge Connection is divided in simple components and the stiffness is calculated analytically. Then verification of the results is performed using Finite element models set up for that purpose.

In order to investigate the behaviour of the combined system in terms of magnitude of reaction force at MP/TP interface, different FEA models have been set up with different position and magnitude of imperfection.

As final step, fatigue analysis is performed based on FEA results for perfect and a preselected imperfect structure. Based on a realistic load spectrum the fatigue damage is estimated for both cases.

## 1.6 Reference geometry

A reference wind turbine structure is selected for the purpose of this thesis based on realistic dimensions. The outer diameter of the tubulars is **xx [mm]**. The thicknesses of the upper shell and lower shell (MP) are selected being equal to **xx** and **xx [mm]** respectively (**Error! Reference source not found.**). As a starting point the maximum line load and structure diameter at a typical MP/TP interface level (ca. 0m LAT) provided by different turbine suppliers is used. The **line load is xx [MN/m]** and the number of segments  **$N_{\text{seg}}=x$** . Bolts **M42 8.8** are used.

## 2 State of the art

As it is already mentioned the C1 Wedge Connection is a totally new connection and uses a different pretension mechanism compared to the Ring flange connection. Also, the flange design differs significantly in geometry from the standard L-flanges. Therefore, the effect of flange waviness due to fabrication and installation tolerances needs to be investigated. In order to be able to do that, it is necessary to calculate the stiffness for the different parts of the connection. For this purpose an analytical method for the stiffness calculation at a Ring flange connection was proposed by M.Seidel [4]. At this chapter the method is described step by step and later it is adapted for the C1 Wedge connection.

### 2.1 Description of method proposed by M. Seidel (2018)

The purpose of this method is to calculate analytically the stiffness of the different parts of the Ring flange connection and verify them using FE-models that have been set up for this purpose.

#### 2.1.1 FE-model description for calculation of shell stiffness

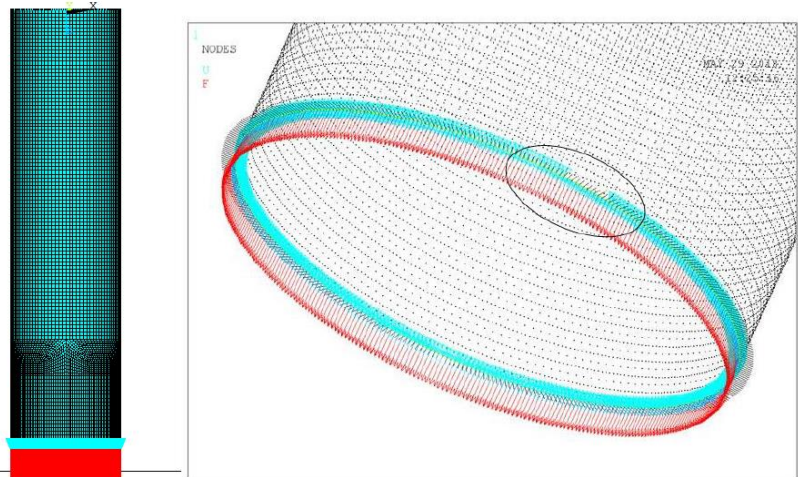
In order to estimate the shell stiffness of the upper part of the connection, a model with the following characteristics has been set up by M.Seidel [4].

- **Geometry**

Specifically, cylindrical shells with three different but constant diameters (4000mm, 6000mm, 8000mm) and wall thickness from 10mm to 100 mm are modelled. The height of the shell is  $H=24\text{m}$  which is a typical section length for tower sections.

- **Boundary conditions**

In order to simulate the gap, certain boundary conditions are used. At the bottom the shell is supported in all translational degrees of freedom and at the part which represents the gap the supports in vertical direction are removed assuming that the circular shape is maintained due to the presence of the flange.



- **Loads**

A line load force is applied along the circumference with magnitude equal to the preload of the bolt times the number of bolts.

### 2.1.2 Results

The deformation 'u' in the middle of the gap section is extracted. Then the linear stiffness of the shell is calculated as:

$$k = \frac{F_v \cdot n}{\pi \cdot D \cdot u}$$

*Equation 1- Linear stiffness calculated from the extracted deformation 'u' from FEA.*

where k is the computed linear stiffness [N/mm/ mm],  $F_v$  is the preload of the bolt [N], n is the number of bolts, D is the diameter of the shell [mm] and u is the deformation in the middle of the gap [mm].

The results are plotted for combinations of different parameters: diameter, wall thickness and gap angles from 10° to 100°.

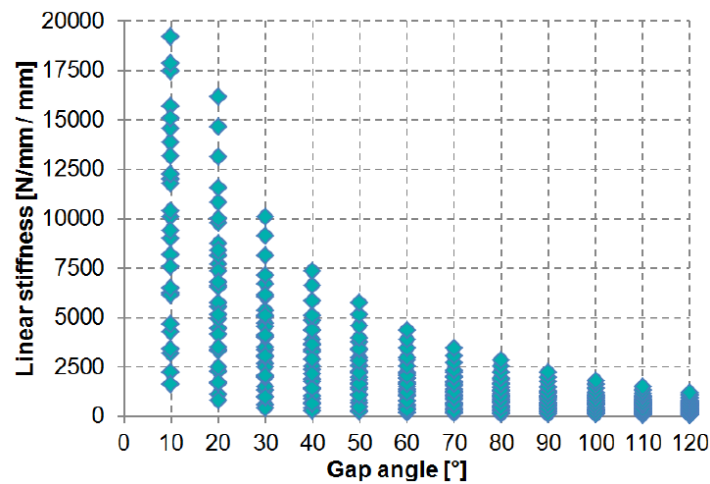


*Figure 2.2- Stiffness vs gap angle for different combinations.*

From the results, the linear shell stiffness estimated by M. Seidel as:

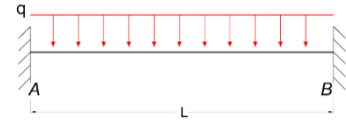
$$k_{shell} = \frac{E \times t_{shell}}{1.8 \times l_{gap}} \text{ [N/mm/ mm]}$$

*Equation 2- Analytical formula for calculation of linear stiffness of the shell.*

where E is the Young's modulus of steel [N/mm<sup>2</sup>],  $t_{shell}$  is the shell thickness [mm] and  $l_{gap}$  the length of the section with gap [mm].

Additionally, the flange itself provides resistance against gap closure. Considering the flange as a double fixed beam, with length equal to the segment which is free to deform, under distributed load the flange stiffness is estimated as:

$$k_{flange} = 384 \times \frac{E \times I_{flange}}{l_{gap}^4}$$



Equation 3- Analytical estimation of TP flange stiffness based on Bernoulli beam theory [N/mm /mm].

where  $I_{flange}$  is the moment of inertia of the beam around the longitudinal axis of the beam [mm<sup>4</sup>].

The total stiffness can be estimated as:

$$k_{total} = k_{flange} + k_{shell}$$

Equation 4- Stiffness of the combined TP.



## 3 Preload mechanism

Preload between the flanges is achieved by a horizontal actuation load on the wedges, which is provided by torquing the bolt. The required actuation load is a function of the slope angle of the inclined planes combined with the static friction between wedges and blocks. The actuation load will be supplied by a bolt and a torque tool. The consequential reaction torque is absorbed by a reaction washer, like those provided by HYTORC. The required preload between flanges is equal to ULS Tensile load. If the friction is lower than expected, a given actuation load will result in more preload than required.

### 3.1 Load path without preload

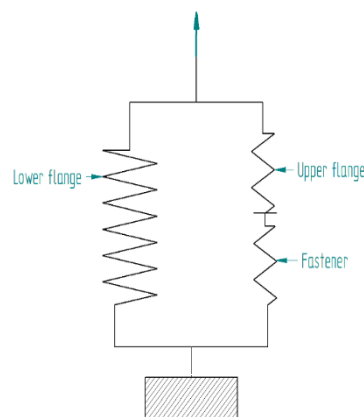
An external compressive force is transferred through the contact plane of both flanges.

An external tensile force is transferred from the upper flange via lower block, wedges and upper flange to the lower flange (**Error! Reference source not found.**)

### 3.2 Load path with preload

A preload wedge connection can be presented as a two parallel spring system with two arms.

- A relatively stiff spring in compression which represents the stiffness of the MP flange (top part above the holes)
- A relatively flexible spring arm with a series of springs which represents the TP flange-fastener assembly.



The inclined plane on both wedges and blocks will transform a horizontal load on the wedge into a preload force in the contact plane of the flanges. An external tensile load will either increase or decrease this contact load. The load change of both springs is proportional to their individual stiffness.

An external load has the following effect on the components:

External load	Contact plane load	Stiff spring load (lower flange)	Flexible spring load (upper flange, wedge and shells)
Tensile direction	Decreases	Decreases	Increases
Compressive direction	Increases	Increases	Decreases

A sufficiently large external tensile force decreases the preload force in the contact surface between upper and lower flange until the two flanges are separated. The effect of an external load on a preloaded lower flange is graphically displayed below. A preloaded lower flange (left) is subjected to a tensile external load (right):

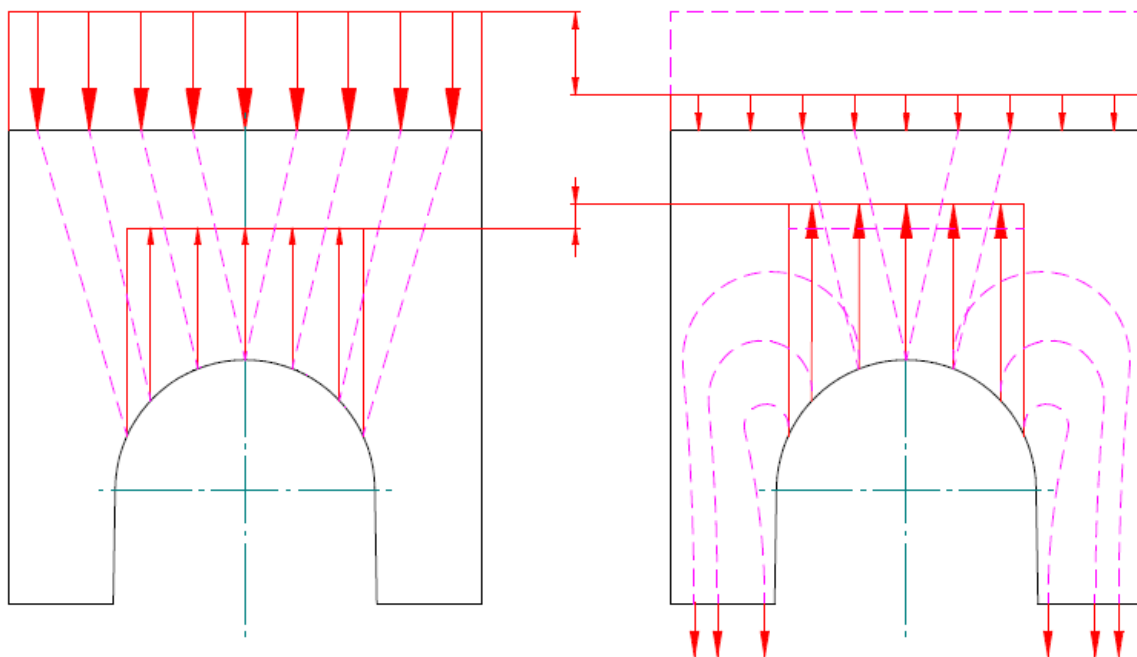


Figure 3.2- Preloaded lower flange subjected to tension.

A preloaded lower flange (left) is subjected to a compressive external load (right):

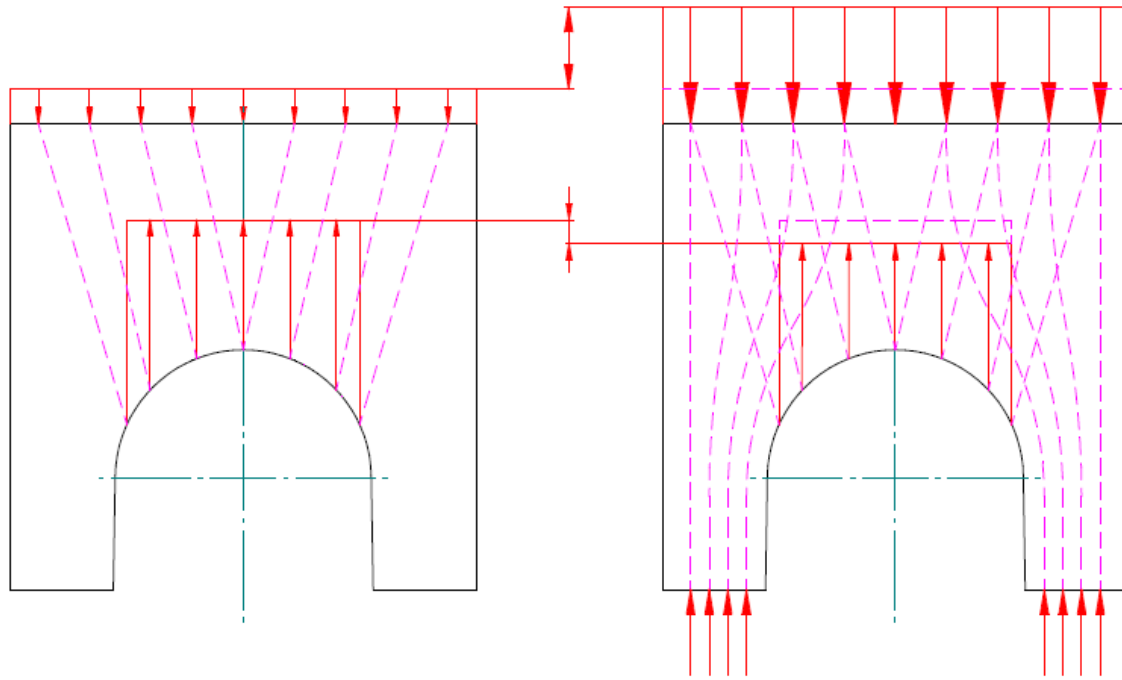


Figure 3.3- Preloaded lower flange subjected to compression.

The load at the contact surface increases while the fastener load decreases marginally. The compressive load is transferred to the sub-structure via the material around the hole in the lower flange.

### **3.3 Spring system stiffness**

The stiffness is verified by FE models for an external load of magnitude ULS tensile load in an un-preloaded assembly.

#### **3.3.1 Stiffness of the top of lower flange (MP stiffness)**

The lower flange is compressed xx mm under a tensile load of xx MN. So, the stiffness is xx MN/mm.

#### **3.3.2 Stiffness of upper flange-fastener assembly (Fastener stiffness)**

The upper flange and the fastener assembly are compressed xx mm under a tensile load of xx MN. The stiffness is xx MN/mm.

### 3.3.3 Overview of results

By applying those stiffnesses to the parallel spring model that described at 3.2, is found that the load distributed ratio between the MP and the Fastener assembly is  $3.2 / (3.2+35) = 8.5\%$ . That means that approximately 8.5% of the total tensile load applied to the parallel spring model is transferred through the TP/fastener assembly. The same result it is represented in following line graph for MP and TP/fastener. For the same deformation applied in both MP and TP/fastener the force transferred by the MP is much larger.

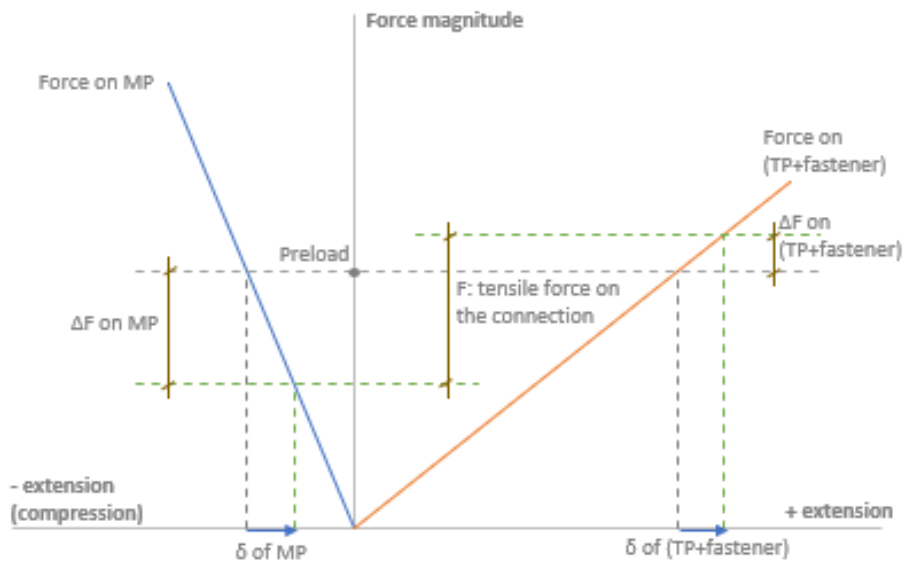


Figure 3.4- Load-displacement diagram preloaded connection.

### 3.4 Calculation of required preload

At the start of this chapter is presented the geometry and the magnitude of external loads that were selected for this certain analysis. The main objective is to define analytically the relation between the horizontal preload (actuation load on the wedges) and the resulted vertical preload between the flanges that is needed at a single segment of the C1 wedge connection in order to counterpoise the ULS external tensile load.

#### 3.4.1 Segment loads

- **ULS Tensile load**

The most critical load direction is in tension. The ultimate tensile segment load is given by:

$$F_{seg} = Q * \frac{\pi * D}{N_{seg}}$$

where Q is the line load (Chapter 1.6) in MN/m, D the outer diameter of the tubulars and  $N_{seg}$  the number of fastener assemblies along the full ring.

- **ULS Compressive load**

Compressive loads are transferred directly from the top to the bottom flange. The ULS compressive segment load is assumed to be the same magnitude at the ULS tensile load:

$$F_{seg,compr} = -F_{seg,tens}$$

#### 3.4.2 Material properties

Component	Material	(Reduced)Yield strength [MPa]
TP flange	S460	360*
MP	S460	440
Fastener/wedge	S690 or equivalent	650
Bolt	Grade 8.8	640

Conservative, high friction coefficient at wedges (lubricated steel-steel):  $\mu=0.15$ .

### 3.4.3 Actuation loads

The target preload between the MP and TP is equal to the Ultimate Tensile segment load which was computed equal to 2.8MN. A free body diagram (FBD) of the wedges expands on the actuation load required (Figure 3.5).

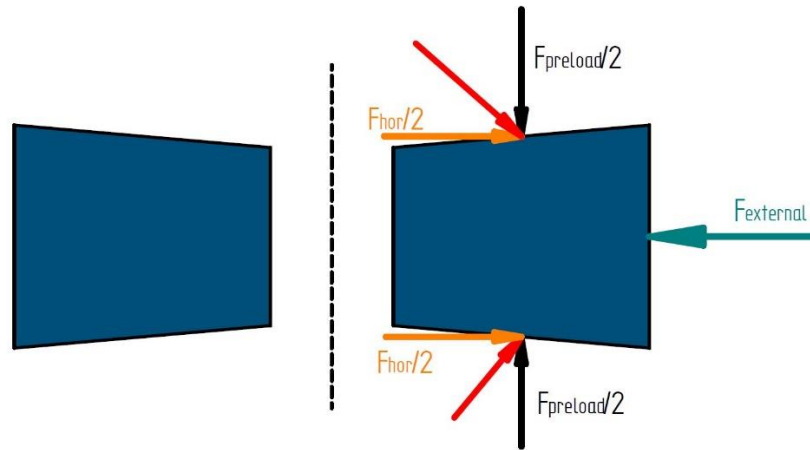


Figure 3.5- Free body diagram of a single wedge, generating half of the required preload. The red arrows, representing normal force to the inclined planes, are in reality perpendicular to the surface.

Each half (left/right) of the fastener assembly supplies half of the preload required. The horizontal component required to provide the preload is:

$$\tan a = \frac{F_{hor} / 2}{F_{preload} / 2} \Rightarrow F_{hor} = \tan(a) * F_{preload} = \tan(5^\circ) \times 2800 = 245 \text{ KN}$$

The horizontal force required to overcome the friction between the wedges and the blocks is:

$$F_{hor} = \mu * F_{preload} = 0.15 \times 2800 = 420 \text{ KN}$$

The total horizontal force required is equal to:

$$F_{hor(total)} = [\tan(\alpha) + \mu] * F_{preload} = 245 + 420 = 665 \text{ KN}$$

If the actual friction is lower than 0.15, additional vertical preload will be generated. The same holds if the bolt would be preloaded to more than 70% of yield. These affects are plotted in (Figure 3.6).

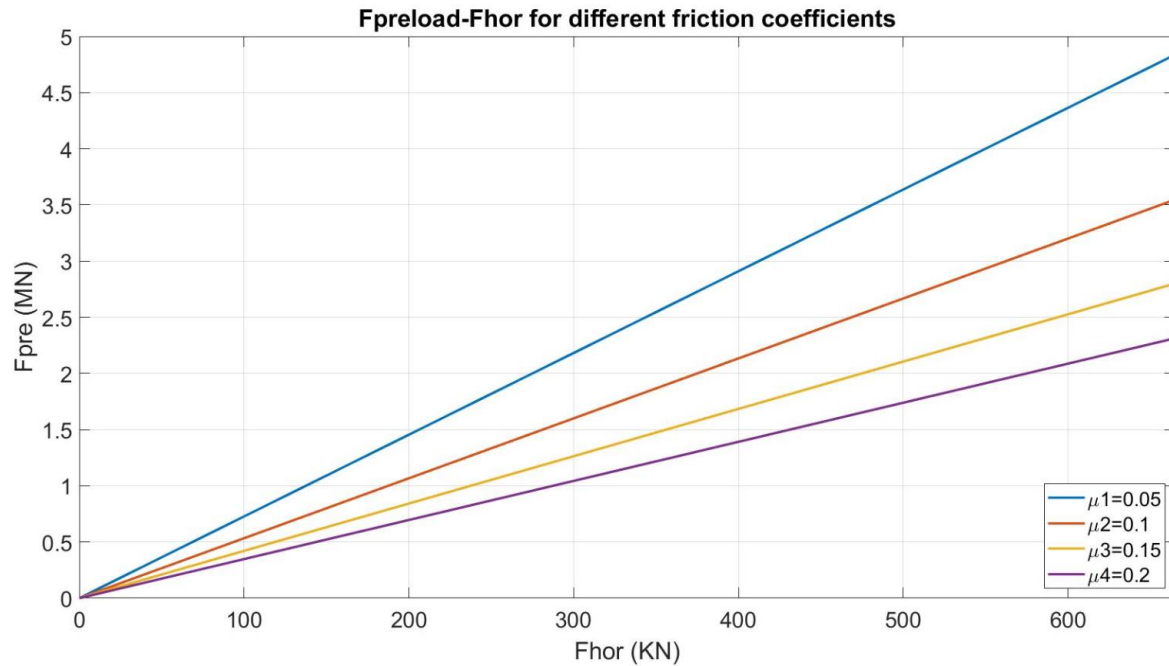


Figure 3.6- Relationship between bolt force ( $F_{hor}$ ) and vertical preload ( $F_{preload}$ ) for different friction coefficients.

### 3.4.4 Self- locking mechanism

If the bolt in some way would fail to provide the required locking force, ideally the wedge should be self-locking in order the preload at the interface to be remained stable. In that case the friction force should always be greater than the horizontal component of a tensile external load, as generated by the inclined plane of the wedges ( $F_{out}$ ). This can be represented by the following expression:

$$F_{friction} \geq F_{out}$$

$$\frac{F_{ULS}}{\cos(\alpha)} * \mu \geq F_{ULS} * \tan(\alpha)$$

Which can be solved for  $\mu$ :

$$\mu \geq \tan(\alpha) \cos(\alpha) = \sin(\alpha)$$

For  $\alpha = x$ . Because the contact is steel-on-steel, it is unlikely that the friction coefficient being lower than this value. Therefore, with a normal friction coefficient, the wedges are self-locking and are not expected to loosen over time, even if the bolt would be completely removed.

## 4 Stiffness approximation of the different parts on the C1 Wedge Connection

The gap closing behaviour of the connection depends on several parameters such as the shape of the gap, length of the gap along the circumference, tower wall (shell) thickness and resulting meridional/bending stiffness, and stiffness - flange geometry. This chapter is focused on the geometry on both flanges (upper flange TP and lower flange MP). The purpose is to split up the connection in parts and then calculate the stiffness of those individual components. The methodology for the derivation of analytical formulas is described step-by-step and FE-models have been set up on ANSYS workbench and mechanical for verification.

### 4.1 Stiffness estimation of individual components of Upper flange TP

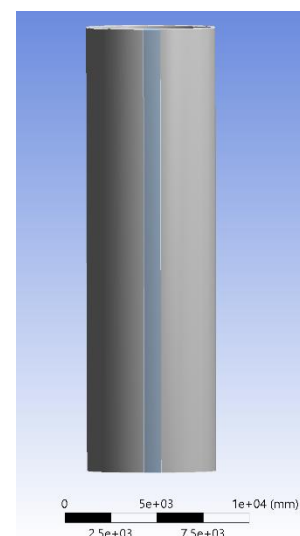
The upper flange TP is composed by two parts, the TP-flange and the TP-shell. Initially the upper flange is split into those two parts and the stiffness for each of the parts is calculated analytically and verified by FE- models built for this purpose. At next step the combined system is verified by the whole upper flange model. At the end the results for all three models are compared with the analytical calculations of stiffness and presented graphically.

#### 4.1.1 Stiffness calculation of TP shell using FE analysis

##### Model description for calculation of TP shell stiffness

###### *Geometry*

In order to estimate the meridional shell stiffness, a materially linear and FE-model (Figure 4.1) has been set up. This model comprises a straight cylindrical shell, with constant diameter of 7 [m] and wall thickness 85 [mm]. The height of the shell was selected equal to  $H=24$  [m] which is a typical section length for lower tower sections.



## 4. Stiffness approximation of the different parts on the C1 Wedge Connection

### Boundary conditions

At the bottom the shell is supported in all translational degrees of freedom around the full circumference (Figure 4.2a). Within the sector of the flange gap which indicated with red circle, the support in longitudinal direction is removed (Figure 4.2b).

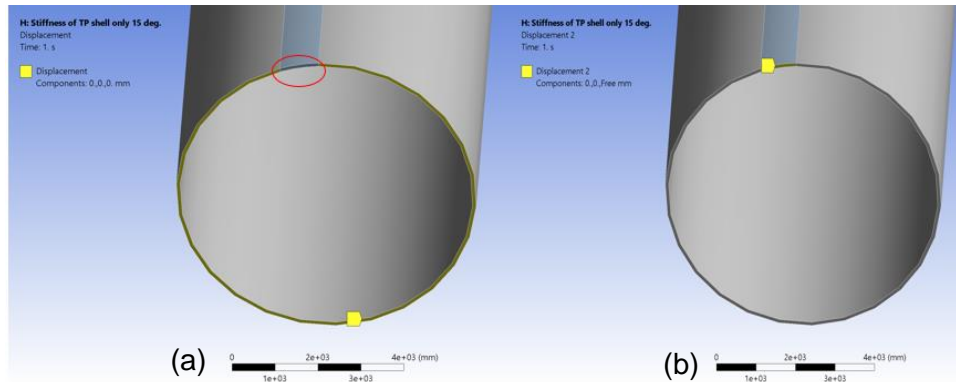


Figure 4.2- Fixed boundary conditions in all translational directions along the circumference (a) and free to deform longitudinally at the segment where the gap is present (b).

### Loads

A line load is applied along the circumference with magnitude equal to the resulting vertical preload force which is 2.8 [MN] times the number of bolts (Figure 4.3).

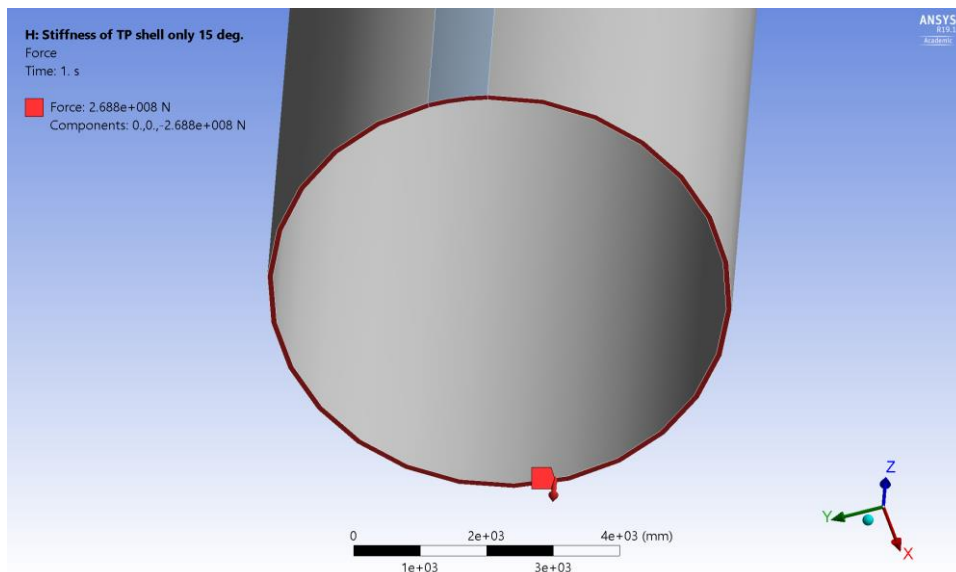


Figure 4.3- Uniform distributed load along the whole circumference of TP shell.

### Materials

All components of the C1 Wedge Connection designed as structural steel. A linear material model is selected, with  $E=200$  [GPa].

### Mesh

At this certain group of analysis, a mesh with 200 [mm] element size is performed along the full length of the TP-shell (Figure 4.4).

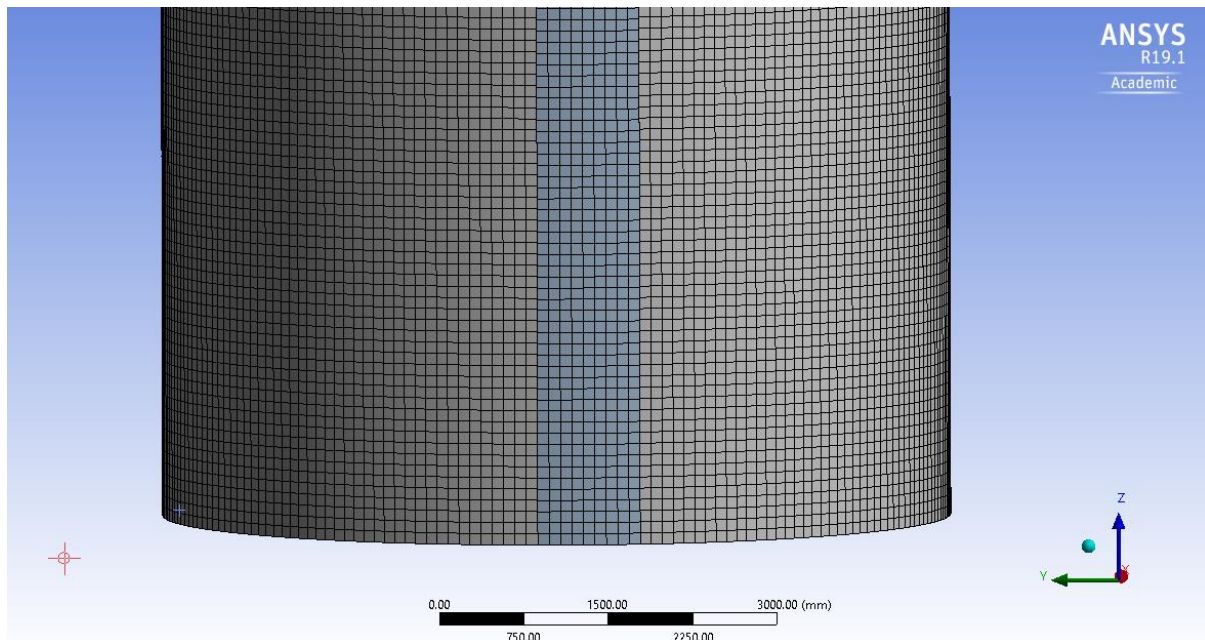


Figure 4.4- Mesh used for this certain group of analysis.

In order to calculate the numerically extracted stiffness of TP-shell, five different models have been set up using the same characteristics as described at the previous section and the only difference the gap size (15, 20, 30, 45, 60 degrees). On these models the deflection “u” in the middle of the gap sector is extracted. The linear shell stiffness is evaluated as:

$$k = \frac{F \times N_{seg}}{l_{gap} \times u} \quad [4]$$

Equation 5- Linear stiffness calculation based on the extracted deformation “u” from FEA in [N/mm/ mm].

where k is the computed linear stiffness [N/mm/ mm], F is the vertical preload to the connection due to bolt preload [N],  $N_{seg}$  is the number of bolts contained in the section we are interested to calculate the stiffness,  $l_{gap}$  is the length of the section with gap [mm] and “u” is the deformation in the middle of the gap [mm].

Results are plotted versus gap angle for the three different gap angles in Figure 4.5 .

## 4. Stiffness approximation of the different parts on the C1 Wedge Connection

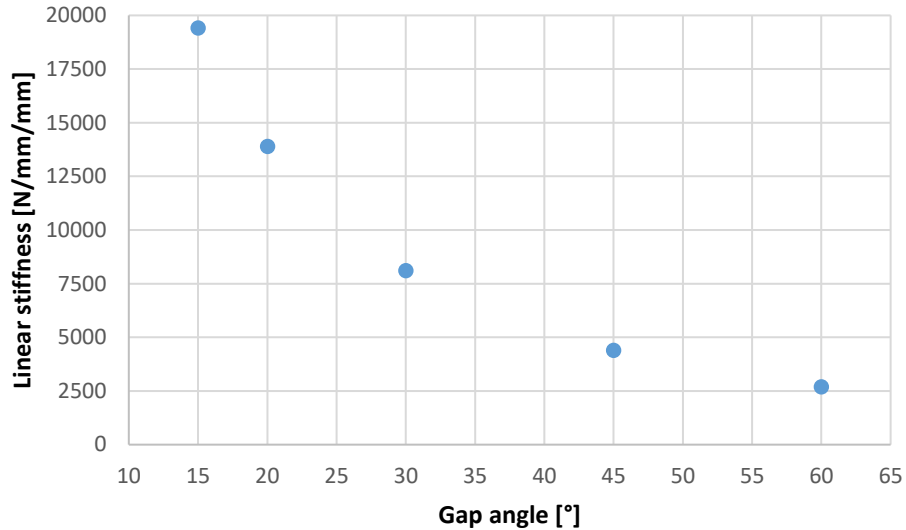


Figure 4.5- Stiffness of TP-shell vs gap angle for all data points of numerical study.

### 4.1.2 Analytical estimation of upper flange shell stiffness

The linear shell stiffness can be estimated using the formula which is the simple axial stiffness of a plate strip having the length of the gap (Equation 6).

$$K_{TP}(shell) = \frac{E \times s}{l_{gap}} \left[ \frac{N / mm^2 \cdot mm}{mm} = \frac{N / mm}{mm} \right]$$

Equation 6- Analytical calculation of TP-shell stiffness.

Where E is Young's modulus  $[N / mm^2]$ , s is the shell wall thickness [mm],  $l_{gap}$  is the length of the gap measured on the circumference [mm].

### 4.1.3 Comparison of analytical and numerical stiffness of TP shell

The quality of this approximation is evaluated in Figure 4.6. Based on these models with five different gap lengths, the overall agreement is good, with stiffness being overestimated by ~5% on average for stiffness larger than 5000 [N/mm /mm]. Significant overestimation of more than 50% on average occurs for small stiffness values (less than ~3000 N/mm mm), but this is noncritical as those belong to very large gaps, which are easily closed.

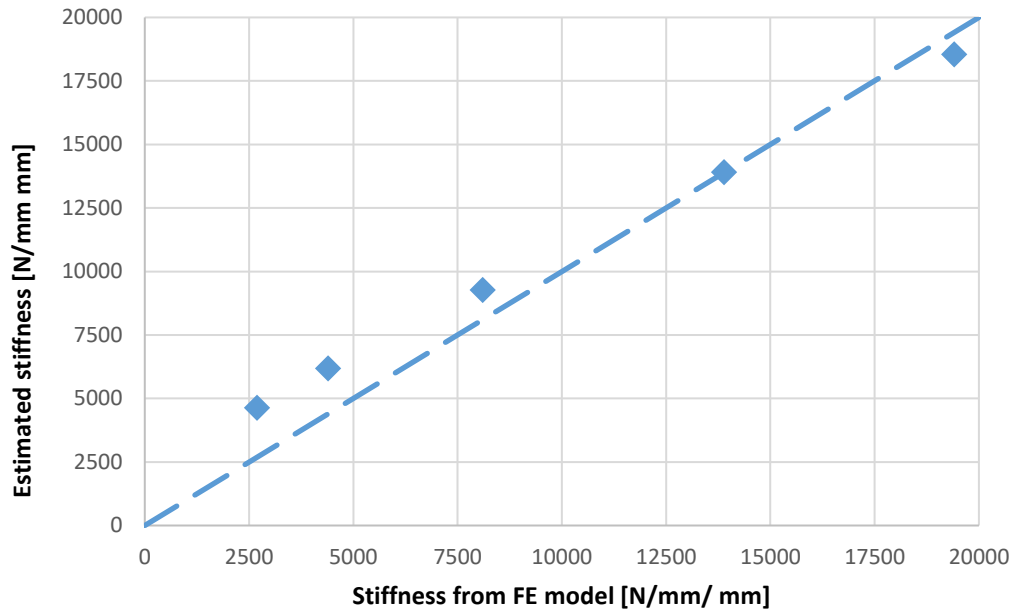


Figure 4.6- Comparison of analytically estimated stiffness vs shell stiffness from FE model.

### 4.1.4 Stiffness estimation of TP flange

As it is already mentioned, the upper flange consists of two components. At this chapter the analytical calculations for the estimation of TP-flange stiffness are presented step by step, from a straight TP flange without holes, till the actual curved TP flange segment with the following geometry (**Error! Reference source not found.**).

As first step we assume a straight TP flange with the same cross section geometry, but without the presence of holes (**Error! Reference source not found.**).

If we consider now the TP flange clamped at both ends, then the deformation of the flange can be estimated using the Timoshenko beam theory which is described analytically in 9 Appendix A. According to this theory the deformation of the beam at the middle ( $x=L/2$ ) can be computed from the following formula:

$$w_{(L/2)} = \frac{q \cdot l^2 (G \cdot A \cdot l^2 + 48 \cdot E \cdot I)}{384 \cdot E \cdot I \cdot G \cdot A} \text{ [mm]}$$

Equation 7- Analytical method for TP-flange (straight model without holes) deflection at the middle of the beam.

#### 4. Stiffness approximation of the different parts on the C1 Wedge Connection

---

where  $q$  is the distributed load [N/mm],  $l$  is the length of the beam [mm],  $GA$  is the shear stiffness,  $E$  is Young's modulus [N/mm<sup>2</sup>] and  $I$  is the second moment of inertia of the flange cross section [mm<sup>4</sup>].

Then the linear stiffness of the entire flange segment can be estimated as:

$$K_{TP\_flange} = \frac{384 \cdot E \cdot I \cdot G \cdot A}{l^2 (GA l^2 + 48EI)} \text{ [N/mm /mm]}$$

*Equation 8- Analytical estimation of linear stiffness of TP-flange (straight model without holes).*

The cross-sectional properties are calculated analytically in 11 Appendix B.

#### 4.1.5 FE Models description for calculation of TP flange stiffness

In order to verify the results of the previous derived formula for the analytical calculation of stiffness for TP flange (Equation 8), three different straight models without holes have been set up on ANSYS software with lengths equal to the respectively curved segments lengths, measured at the circumference. Specifically, the models used for this analysis have lengths 916 [mm], 1831 [mm] and 2749 [mm] which correspond to 15°, 30°- and 45°-degrees curved segments respectively. Their characteristics are presented below.

##### **Boundary conditions & Loads**

As boundary condition for this analysis used the fixed support applied at both ends of the beam (Figure 4.7a) in order to simulate the same static system as it is calculated from the analytical method. The load is applied at both inner surfaces of the beam (Figure 4.7b) instead of the top surface as this position is closer to the centroid axis of the beam. The magnitude of the distributed load is 12 MN/m which resulted by the preload applied on each hole.

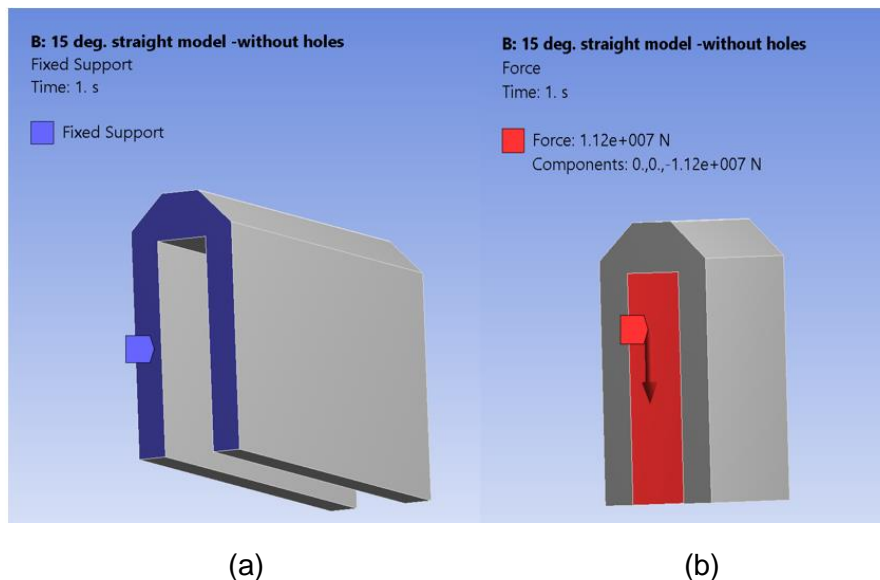
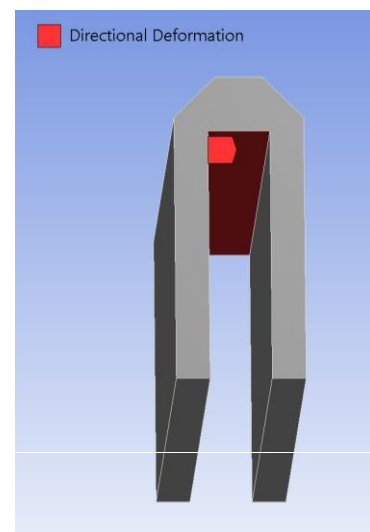


Figure 4.7- Boundary conditions and position of the load.

The deformation at the middle of the beam is extracted, at the surface which is located 450 [mm] from the bottom of the beam (Figure 4.10). The results for the beams with three different lengths are presented at the table 1.



## 4. Stiffness approximation of the different parts on the C1 Wedge Connection

At the second step the same straight beam models are used with the only difference the presence of holes (**Error! Reference source not found.**). This is a more realistic simulation of the actual TP-flange segments.

At this analysis the same magnitude of load is applied but the position is at the lower curved part of the holes. This is also the position where the preload is applied in the real structure (Figure 4.9).

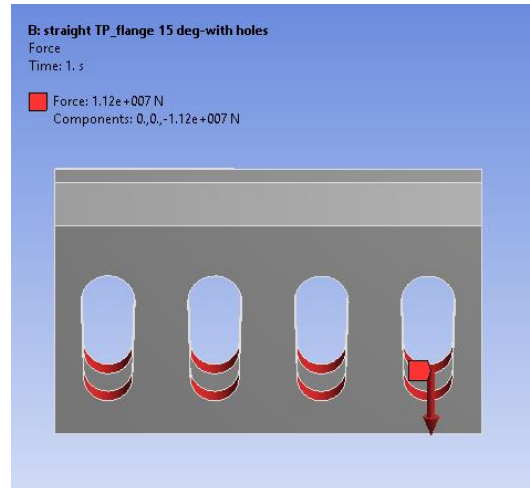


Figure 4.9- Position and magnitude of load used at the second step.

As third step the actual curved TP flange is analysed. The cross section of the TP-flange is the same as in second step but on this analysis the models are curved as they are parts of the full TP flange with outer diameter 7 [m] (**Error! Reference source not found.**). The same magnitude and position of the load is used.

#### 4.1.6 Comparison of analytical and numerical extracted deflection of TP flange for all three approaches

The results for all three aforementioned analysis regarding the deflection at the middle of TP flange are summarized at the following Table 1.

Table 1- Vertical deformation at the middle of the beam for three different geometries and for three different lengths.

Length [mm]	Deflection w [mm] at x=L/2				
	Straight beam without holes (FEA)	Straight beam without holes (Analytical Equation 7)	Straight beam with holes (FEA)	Actual curved TP flange (FEA)	TP flange (Analytical based on Equation 9)
916 (15° equiv.)					
1831 (30° equiv.)					
2749 (45° equiv.)					

Comparing the results from the Table 1 (straight beam without holes and straight beam with holes) we can see that the presence of holes increases the vertical deformation with a factor ~2.5. No significant differences in the deformations are observed between the straight beam with holes and the curved beam based on the numerical results for lengths smaller than 30°. For larger lengths the influence of the curvature becomes critical, increasing the divergence between the straight and curved TP flange more than 10%.

#### 4.1.7 Analytical estimation of TP flange stiffness

Based on numerical results from Table 1 for the beam with and without holes, the directional deformation at the middle of the TP flange with holes can be estimated analytically from the following formula (Equation 9).

$$w_{(l/2)} = 2.5 \times \frac{q \cdot l^2 (G \cdot A \cdot l^2 + 48 \cdot E \cdot I)}{384 \cdot E \cdot I \cdot G \cdot A} \text{ [mm]}$$

Equation 9- Analytical formula for estimation of deflection at the middle of a straight TP flange beam with holes.

At this point no further analysis has been done at the analytical method in order to define the second moment of inertia and the shear area of the TP flange due to the presence of holes.

Then the linear stiffness of the entire TP-flange segment can be estimated as:

$$K_{TP\_flange} = \frac{1}{2.5} \times \frac{384 \cdot E \cdot I \cdot G \cdot A}{l^2 (G A l^2 + 48 E I)} \text{ [N / mm / mm]}$$

Equation 10- Analytical estimation of linear stiffness of TP-flange (straight model with holes).

## 4. Stiffness approximation of the different parts on the C1 Wedge Connection

---

where  $l$  is the length of the beam [mm],  $GA$  is the shear stiffness of the full TP flange cross section without holes,  $E$  is Young's modulus [N/mm] and  $I$  is the second moment of inertia of the flange cross section without holes [mm<sup>4</sup>] (**Error! Reference source not found.**). The factor **2.5** in the denominator has been chosen to consider the presence of holes and the curvature of the TP flange.

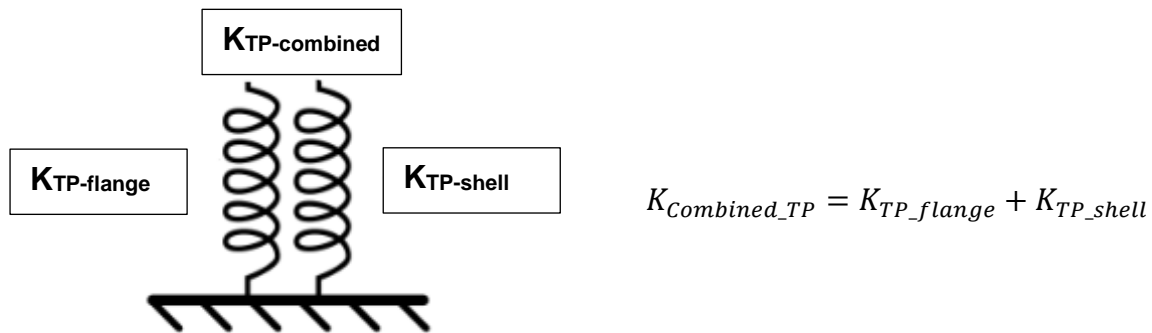
### 4.1.8 Comparison of linear stiffness of TP flange estimated analytically vs numerical results

At the following graph the two curves represent the linear stiffness of TP flange estimated analytically for a straight beam with the cross section of TP flange with holes (Equation 8) and without holes (Equation 10). The numerical results for the three different beam geometries and for three lengths are represented as point markers. The comparison of analytical vs numerical results is presented at the figure below (**Error! Reference source not found.**).

As it is clear from the graph, the estimation of the stiffness of a straight TP-flange without holes has good accuracy with respect to numerical results. The same can be stated for the TP-flange with holes and the actual curved TP flange.

## 4.2 Stiffness estimation of combined Upper flange (TP)

As it is already mentioned in the start of this chapter, the upper flange (TP) is a combined system comprised by two main parts the TP-shell and TP-flange. The stiffnesses of those separate parts were calculated analytically using the Equation 6 and Equation 10 derived at the sub-sections 4.3.2 and 4.3.4 respectively. The Upper flange can be presented as a parallel spring system between the TP-flange and TP-shell [4]. This can be stated as the two parts are deformed together, and no separation is possible. In that case the combined stiffness can be calculated as follows:



Based on the above formula, the analytical equation for the linear stiffness approximation of the combined upper flange (TP) is:

$$K_{combined\_TP} = \frac{1}{2.5} \times \frac{384 \cdot E \cdot I \cdot G \cdot A}{l_{gap}^2 (GA l^2 + 48EI)} + \frac{E \times s}{l_{gap}} \text{ [N/mm/ mm]}$$

Equation 11- Analytical formula for calculation of combined TP linear stiffness.

Stiffnesses of the different TP components, based on analytical calculations are compared at the following Table 2. As it is obvious, dominant component regarding the combined stiffness is the TP-shell.

Table 2- TP flange vs TP shell stiffness comparison based on analytical calculation.

Length [°]	Linear stiffness [N/mm/ mm]		
	TP flange (Equation 10)	TP shell (Equation 6)	Combined TP (Equation 11)
15			
20			
30			
45			

### 4.2.1 FE model description for the combined TP stiffness verification

In order to verify the previous formula (Equation 11) for the stiffness approximation of the combined TP, four different models have been set up on ANSYS software with different gap lengths or gap angles (15°, 20°, 30°, 45°). The characteristics of these models are described below:

#### Geometry

The models are consisting of the TP flange and a straight cylindrical shell with constant outer diameter of  $x$  [m] and wall thickness  $x$  [mm]. The height of the shell was selected equal to  $H=x$  [m] which is a typical section length for lower tower sections (**Error! Reference source not found.a**).

#### Load

At this analysis the resulting vertical preload which is equal to  $x$  [MN] times the number of bolts is applied at the bottom curved parts of TP flange (**Error! Reference source not found.b**) around the full circumference.

#### Boundary conditions

The same boundary conditions are used with the model described analytically in Chapter 0. At the bottom the TP flange is supported in all translational degrees of freedom around the full circumference and at the segment where we are interested to get the deformation (**Error! Reference source not found.b** indicated with light blue colour), the support in longitudinal direction is removed.

#### Results

The longitudinal deformation at the middle of the segment is extracted and the linear stiffness is calculated according to the Equation 5. The results for all cases are summarized and compared with the analytical method (Equation 11) at the following Table 3. The stiffness of combined TP is overestimated by ~28% on average for segment lengths <45°. For larger segments the overestimation is larger than 40% since in analytical formulas is not considered the curvature of the TP-flange which becoming more critical regarding the deflection at the middle.

Table 3- Comparison of linear stiffness of combined TP extracted from FEA vs analytical method for four different gap angles.

Length [mm]	Linear stiffness from FEA [N/mm/ mm]	Analytically estimated Linear stiffness [N/mm/ mm]	Divergence [%]
916 (15° equiv.)			
1221 (20° equiv.)			
1831 (30° equiv.)			
2749 (45° equiv.)			

#### 4.2.2 Magnitude of stresses on TP shell

Since all analytical formulas derived for the stiffness approximation of combined TP (Equation 11) are based that the material (structural steel S460) during deformation stays at the elastic region, a thing which is of particular interest is the stress magnitude at the TP shell at the segment that is free to deform longitudinally. From FE analysis for four different segment lengths (or angles) which characteristics were described at the previous chapter, the magnitude of equivalent von-Mises stress is extracted. At the following figure the contour plot of stresses is presented for the largest segment 45° (**Error! Reference source not found.**), as for smaller segments the magnitude of stresses is lower. From the following plot it is clear that only a very small area is close to the yield limit. Thus, can be stated that the TP shell stays at the elastic region and the extracted results used for verification of analytical formulas are valid.

Based on the figure above, the height of the affected TP shell height due to longitudinal deformation of the imperfect segment is measured, for three different gap lengths (15°, 30° and 45°). As affected shell height it is assumed the distance from the TP-flange/TP-shell interface until the point where the shell stress is larger than 50 [MPa] (**Error! Reference source not found.**). The ratio between the affected shell height (B) and the gap length (A) for the three cases is presented at the following Table 4.

Table 4- Ratio of gap length vs affected TP shell height.

Length [mm]	Affect height of TP shell [mm]	Ratio B/A [-]
916 (15° equiv.)		
1831 (30° equiv.)		
2749 (45° equiv.)		

### 4.2.3 Conclusions for combined TP stiffness approximation

The quality of approximation is evaluated in **Error! Reference source not found.**. The linear stiffness of the Upper flange (TP) estimated analytically is plotted for gap angles from 10 to 50 degrees and at the same graph the numerical results from Table 3- Comparison of linear stiffness of combined TP extracted from FEA vs analytical method for four different gap angles are positioned. Based on the FE models with four different gap angles the overall agreement is good with stiffness being overestimated by ~30% on average. Based on the previous analysis, it has been proven that the accuracy of stiffness estimation based on analytical method is good for both parts TP-shell and TP-flange as individual components of combined TP (Figure 4.6, **Error! Reference source not found.**). The resulting overestimation of the combined TP stiffness caused by the assumption that the behaviour of the combined TP flange is described by a perfect parallel spring system. Regarding the gap closing behaviour of the structure, this is conservative as the actual stiffness is smaller than predicted and the maximum closeable gap is larger.

### 4.3 Stiffness of Lower flange (MP)

#### 4.3.1 Model description for calculation of MP stiffness

The Lower flange (MP) of C1 Wedge Connection is a straight cylindrical shell with constant diameter  $x$  [m] and thickness  $x$  [mm]. The main difference compared to TP shell is the presence of holes at the top part of the shell close to the MP-TP interface (**Error! Reference source not found.**). Following, the differences and characteristics of FE models compared with the TP shell FE analysis described in Chapter 4.1.1, are described below.

##### **Boundary conditions**

The same boundary conditions are applied at the top surface of MP as the lower surface of TP shell. Additionally, a fixed support is applied along the full circumference of bottom MP surface, which is 24 [m] below the TP-MP interface (**Error! Reference source not found.**).

##### **Load**

The same magnitude of the load is applied at these models with only difference the position. At Lower flange (MP) the load is applied at the top curved part of each hole along the full circumference which is the (**Error! Reference source not found.**).

#### 4.3.2 Stiffness calculation of MP stiffness using FE analysis

Using the method described on Chapter 4.1.1 the linear stiffness [N/mm /mm] is calculated using the longitudinal deformation at the middle of the segment extracted from FE analysis. Five models have been set up for that purpose with different gap angles (15°, 20°, 30°, 45°, 60°).

Results are plotted versus gap angle for the five different gap angles in Figure 4.11.

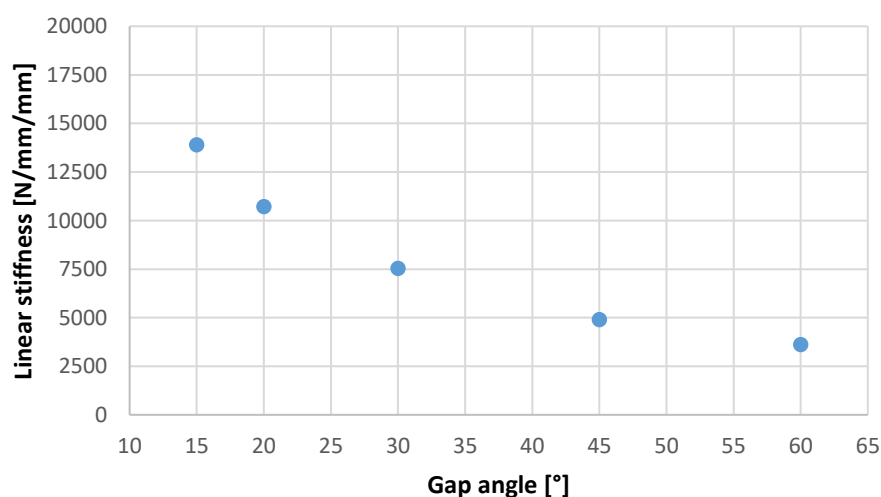


Figure 4.11- Stiffness of MP vs gap angle for all data points of numerical study.

### 4.3.3 Analytical estimation of MP stiffness

The linear shell stiffness can be estimated analytically as:

$$K_{TP}(shell) = \frac{E \times s}{1.5 \times l_{gap}} \left[ \frac{N / mm^2 \cdot mm}{mm} = \frac{N / mm}{mm} \right]$$

*Equation 12- Analytical calculation of MP stiffness.*

where E is Young's modulus  $[N / mm^2]$ , s is the shell wall thickness [mm],  $l_{gap}$  is the length of the gap measured on the circumference [mm].

The formula (Equation 12) is simple the axial stiffness of a plate strip having the length of the gap. Based on FEA results, the factor **1.5** in the denominator has been chosen such that the stiffness is generally overestimated. The formula that describes the stiffness of TP-shell (Equation 6) cannot be used in the case of MP flange. Due to the presence of holes at the top part, the stiffness of MP is reduced.

### 4.3.4 Conclusions for MP stiffness

The quality of this approximation is evaluated in Figure 4.12 and **Error! Reference source not found.**. Based on these models with five different gap lengths, the overall agreement is good, with stiffness being overestimated by ~3% on average for stiffness larger than 10000 [N/mm /mm].

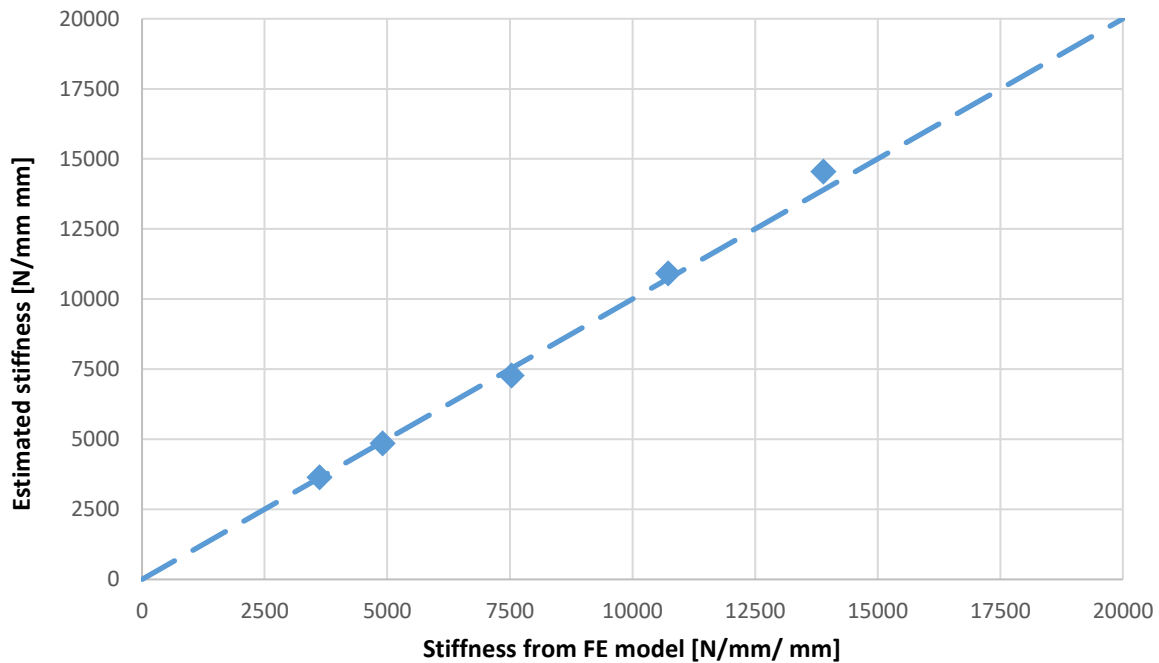


Figure 4.12- Comparison of analytically estimated stiffness vs MP stiffness from FE model.

## 4.4 Maximum closeable gap based on component stiffness

At this chapter a method proposed by M. Seidel is adapted for the C1 Wedge Connection. Using the formulas derived at the Chapter 4 for the analytical approximation of stiffness for all individual component of the connection, the maximum gap that can be closed from this certain geometry is calculated. Initially the methodology is described step-by-step for the certain geometry with a preselected gap length and then is generalized for different gap lengths.

#### 4.4.1 Analytical calculations adapted for the certain case of 15 degrees imperfect segment

The linear stiffness of upper flange TP for an imperfect segment 15° using the data from Appendix B & C can be estimated as:

$$K_{TP} = \frac{1}{2.5} \times \frac{384 \cdot E \cdot I \cdot G \cdot A}{l_{gap}^2 (GA l^2 + 48EI)} + \frac{E \times s}{l_{gap}}$$

The linear stiffness of lower flange MP for the same imperfect segment 15° is:

$$K_{MP} = \frac{E \times s}{1.5 \times l_{gap}}$$

The largest gap that can be closed from each component is calculated as:

$$u_{max} = \frac{P}{k_{total}}$$

where p is the line load induced by the preload:

$$p = \frac{N_{segment} \times F_{preload}}{l_{gap}}$$

where  $N_{seg}$  is the number of fastener assemblies contained in the gap section,  $F_{pre}$  is the vertical preload to the connection due to bolt preload [N] and  $l_{gap}$  is the length of the imperfect segment.

For the upper flange TP, the deformation can be calculated as:

$$u_{max,TP} = \frac{P}{K_{TP}} \text{ [mm]}$$

For the Lower flange MP, the deformation at the middle of imperfect segment can be estimated equal to:

$$u_{max,MP} = \frac{P}{K_{MP}} \text{ [mm]}$$

## 4.5 Conclusions

This analytical method which was described above has been applied for gaps with lengths between 0 and 5.5 [m] (or 0 to 90°). The friction coefficient between the components is

#### 4. Stiffness approximation of the different parts on the C1 Wedge Connection

---

selected being equal to  $\mu=0.15$  which has been proved from experiments performed at TU Delft lab that is conservative [14]. The resulting relation between maximum deformation by the lower flange (MP) and the upper flange (TP) versus the gap length (in degrees) is plotted (**Error! Reference source not found.**). Regarding the total system (grey curve) cannot be stated that the maximum gap that can be closed is the simply add of the individual MP & TP deformations, because due to progressive closing of the gap, the combined system has a higher stiffness. An estimation for the maximum closeable gap of the combined system is the average of MP and TP deformation.

#### 4. Stiffness approximation of the different parts on the C1 Wedge Connection

## 5 Behaviour of imperfect structure

At this chapter the behaviour of a full structure is analysed considering the interaction between the upper flange (TP) and lower flange (MP) assuming pre-described imperfections in the main parts of the connection. In order to analyse numerically the behaviour of an imperfect structure, different FE-models have been set up on ANSYS software. With this certain analysis, firstly we can describe the behaviour of the connection in the section that contains the imperfection. This is analysed through the gap closing procedure. Secondly and high importance is the calculation of the reaction force at the segment of the imperfect part where the maximum gap height is appeared (most critical segment). The resulted reaction force is compared with the maximum reaction force in case of a perfect structure during the preloading and application of external loading phase. At the end, two full structures with different pre-selected gap sizes based on maximum closeable gap estimation (**Error! Reference source not found.**) are analysed. The results for different position of the imperfection are presented graphically for both loading phases.

### 5.1 FE Analysis single segment- Model description

In order to understand the behaviour of an imperfect structure and compare it with a perfect one, the reaction force at the contact surface between the MP and TP for a perfect single connection is calculated. Two different single segment FE-models were built on ANSYS with the only difference the way that the preload is applied. In the 1<sup>st</sup> model the resulted vertical preload is applied directly on the flanges while in the 2<sup>nd</sup> model is applied as two horizontal loads on both wedges pulling them together (**Error! Reference source not found.**).

#### 5.1.1 Geometry

Two single segments of the design of the C1 Wedge Connection are modelled (**Error! Reference source not found.**). Both segments are curved according to the diameter of the TP ( $x$  m outer diameter). Above and below the connection itself,  $x$  [m] of additional shell has been modelled in order to take into account a representative stiffness of them and to avoid any local boundary condition issues (**Error! Reference source not found.**). At the first model the fastener assembly is not modelled while in the second one, the fastener assembly is modelled but without the bolt for model simplification. Based on the analytical model, no specific attention is required for these components at this certain analysis.

### 5.1.2 Contacts

Contact surfaces are defined between the following components. The type of contact and friction coefficient are presented in Table 5.

Table 5- Contact definitions FE model.

Contact	Target	Type	$\mu$
Upper flange	Lower flange	Frictional	
Lower flange	Upper flange	Frictional	
Upper flange	Lower flange	Frictional	
Upper flange	Wedges	Frictional	
Lower flange	Wedges	Frictional	

### 5.1.3 Materials

All components of the C1 Wedge Connection designed as structural steel. A linear material model is selected, with  $E=200$  GPa.

### 5.1.4 Boundary conditions

A fixed boundary condition is applied to the bottom of the lower flange, which is  $x$  m below the interface to the upper flange. Cyclic symmetry is used to model the ring stiffness of the structure. To this end, symmetry boundary conditions are applied to the sides of the segment model, on both upper and lower flange (**Error! Reference source not found.**).

### 5.1.5 Loads

Different loads are applied between those models in order to describe the preloading. At the model without the fastener assembly the resulted preloading is applied to the inside top curved part of MP hole with magnitude  $F_{pre}=x$  [MN] and at each lower curved parts of TP holes with magnitude  $x$  [MN] each. At the second model with the fastener assembly, the preloading  $F_{actuate}=x$  [KN] is applied to the inside of the hole on the outer wedge and to the outer area of the inner wedge, pulling them together (**Error! Reference source not found.**).

### 5.1.6 Mesh

Automatic mesh is performed with “fine” relevance center. Additionally, the mesh is refined for the entire model with 35 [mm] goal elements size (**Error! Reference source not found.**). No

locally refined mesh is used on these models because they are built in order to calculate the reaction force at the contact surface between the flanges. No significant differences are expected using finer mesh.

## 5.2 Maximum reaction force verification

The resulting reaction force at the interface between MP and TP for both cases is plotted versus the resulting vertical preload with maximum value at  $x$  [MN] which represents the maximum preload (**Error! Reference source not found.**).

As it is clear from the following graph, the resulting reaction force is almost the same for both models. Thus, at the following analysis for simplification, we can use the model without the fastener assembly.

## 5.3 FE analysis of imperfect full ring structure - Model description

In order to investigate the behaviour of an imperfect full ring structure, different FE-models have been set up. The purpose of this analysis is to be able to calculate the magnitude of the gap and the reaction force at the most critical segment during preloading phase and during application of external load. Following, the certain characteristics of FE-models are described.

### 5.3.1 Geometry

Two main FE-models with full ring of the C1 Wedge Connection have been set up with a pre-described imperfection and the only difference the magnitude of the gap (gap length/angle & gap height). Specifically for the first main model a gap segment 30 degrees with  $x$  [mm] height at the middle is selected and for the second one an imperfect segment of 15 degrees with  $x$  [mm] (**Error! Reference source not found.**).

The outer diameter of both upper flange (TP) and lower flange (MP) is  $x$  [m]. Above and below the connection itself,  $x$  [m] of additional wall has been modelled to take into account the stiffness of the shell and top avoid any local boundary condition issues. The fastener assembly is not modelled in order to simplify the model based on the reaction force verification (Chapter 5.2).

For each of the two main-models, three different cases are analysed with the same height of the gap at the middle of imperfect section. The only difference is the position of the imperfect section among the connection parts. Namely are:

- a) Perfect TP, gap on lower flange (MP) (**Error! Reference source not found.a**)
- b) Gap on upper flange (TP), perfect MP (**Error! Reference source not found.b**)
- c) Gap evenly divided between both flanges (**Error! Reference source not found.c**).

### 5.3.2 Materials

All components of the C1 Wedge Connection designed as structural steel. A linear material model is selected, with  $E=200$  GPa.

### 5.3.3 Contacts

Contact surfaces are defined between the following components. The type of contact and friction coefficient are presented in Table 6.

Table 6- Contact definitions FE model.

Contact	Target	Type	$\mu$
Upper flange(perfect)	Lower flange(imperfect)	Bonded	
Lower flange(perfect)	Upper flange(imperfect)	Bonded	
Upper flange	Lower flange	Frictional	

### 5.3.4 Mesh

Automatic meshing is performed with 'coarse' relevance center and 5000 [mm] goal element size (**Error! Reference source not found.**). The mesh is refined around the following contact areas which are the most interested in this certain analysis:

- Upper to lower perfect flange – 35 [mm]
- Upper to lower imperfect flange – 35 [mm]

### 5.3.5 Boundary conditions

A fixed boundary condition is applied to the bottom of the lower flange (MP) which is 15 [m] below the contact surface between MP and TP flanges.

### 5.3.6 Loads

Two load steps are defined:

1. Preloading: apply the resulting vertical preload  $F_{pre}=x$  MN in every connection of the full ring to the top curved part of the MP hole and  $x$  MN at each of two lower curved parts of the TP holes (Figure 5.1).
2. 50% ULS tensile: the actuation load is maintained, while an external bending moment is applied to the top of the upper flange (TP) with magnitude  $x$  N\*mm, aligned such that the imperfect segment experiences the maximum tensile load at the middle (**Error! Reference source not found.**).

Figure 5.1- Preload for lower (left) and Upper flange (right).

## 5.4 Results

For this analysis of both main models with 15- and 30-degrees imperfect section, three different FE-models are used as described in Chapter 5.2. In two out of the three sub-models, the imperfect section is positioned only at one flange TP or MP. The third FE-model is a combination of the previous two, with gap evenly divided between both flanges but with the same gap height at the middle of imperfect section. In order to be able to read out the resulted reaction force, the top surface of the imperfect segment is divided in separate areas. The reaction force at the middle segment is extracted, as it is the most critical.

### 5.4.1 FE Analysis of structures with imperfect section 30° and gap height x mm

The analysis was done in two steps. In the first step the preload until the maximum allowable magnitude is applied and in second step we apply the resulting bending moment (Chapter 5.3.6). The magnitude of the gap at the middle of the imperfect section is measured at the end of both steps and the results are summarized in the following table for all cases (Table 7).

Table 7- Magnitude of the gap for all three cases after the end of the two loading steps.

<u>Position of Imperfect section</u>	<u>Magnitude of the Gap</u>	
	After preloading [mm]	After 50% ULS External Load [mm]
Only at MP with perfect TP		
Only at TP with perfect MP		
On TP&MP		

#### **Reaction force at the most critical position**

The connection which is the most interested and critical is positioned in the middle of the imperfect segment. In order to have a clear view for the behaviour of this critical connection, the reaction force at this position is calculated through the FE-Analysis for the three aforementioned cases. Specifically, in the first graph the resulting reaction force expressed as a percentage of the maximum reaction force that we can have in the contact surface of both flanges (TP&MP) which is found being equal to xMN. The comparison of the three different cases of imperfect structures during the preloading phase is displayed below (**Error! Reference source not found.**). As it is clear from the graph, till the point of **1.8 [MN]** preload force, the reaction force at the MP/TP interface is zero as the gap is still open. From this point, the gap closes and the contact force starts to increase for the case of imperfect TP only and evenly divided imperfection at MP&TP. In case of imperfect MP only the gap closes later under 2.1 [MN] preload and after application of the maximum preload cannot reach the same contact force compared to the other cases.

During the application of external bending moment (2<sup>nd</sup> step), the resulting reaction force at the most critical connection of the structure expressed as a percentage of the maximum reaction force that we can have at the contact surface of both flanges. The resulting reaction force is plotted during the application of external load that was selected in this certain case being equal to  $x$  MN which represents the 50% ULS tensile load per segment. The results of this analysis for the three cases are represented and compared in the following graph (**Error! Reference source not found.**).

From the graph after application of the external tensile load, the gap at MP/TP interface starts open again and for all cases the reaction force decreases. Specifically, for the case of imperfect MP, the gap fully opens under 0.5 [MN] tensile load and then reaction force is turned to zero. In the same way the gap fully opens at the point when  $x$  [MN] tensile load is reached for the other two cases.

### 5.4.2 FE analysis of structures with imperfect section 15° and gap height 0.5mm

The same procedure was applied for an imperfect section 15 degrees with the selected height of the gap being equal to  $x$  [mm] at the middle. As in the previous analysis, three different cases were analysed regarding the position of the imperfect section in the different parts of the structure. Applying the same preload and 50 % ULS external tensile load we get the following results concerning the magnitude of the gap at the imperfect segment for both steps (Table 8).

Table 8- Magnitude of the gap for all cases after the end of the two loading steps.

<u>Position of Imperfect section</u>	<u>Magnitude of the Gap</u>	
	After preloading [mm]	After 50% External ULS Load [mm]
Only at MP with perfect TP		
Only at TP with perfect MP		
On TP&MP		

The results regarding the magnitude of the reaction force at the most critical segment of the imperfect section during both loading stages are summarized and compared to the following graphs (**Error! Reference source not found., Error! Reference source not found.**).

From this graph it is obvious that the gap closes at an earlier stage compared to the previous imperfect geometry (30° with  $x$  mm gap). When a tensile load of  $\sim 0.4$  [MN] is reached, the gap is fully closed first for the case of imperfect TP. Followed by the case of imperfect MP&TP at 0.7 [MN] preload and last the gap fully closes under 0.9 [MN] preload for the case of imperfect MP.

During the application of external tensile load, the gap remains closed for all three cases until the 50 % ULS tensile load is reached (**Error! Reference source not found.**). Additionally, the rate of reduction for the reaction force is the same.

## 6 Fatigue calculation of imperfect structure

The main goal of this chapter is to predict stresses on the selected imperfect connection and calculate the fatigue damage at the most critical positions compared to the perfect one. For that reason, detailed FE models of the full-scale perfect & imperfect geometry of the connection were built. According to experiment results that have been done at TU Delft for a scaled single segment model of the C1 wedge connection (**Error! Reference source not found.**), the most critical part of the connection for crack initiation is the MP flange and specifically at the position where the top curved part of the hole is started (**Error! Reference source not found.**). Thus, the following analysis for the full perfect and imperfect structure will be focused on the MP flange.

### 6.1 FE modelling - Single segment reference model

A detailed FE model of single segment was used to predict stresses (**Error! Reference source not found.**) and compare these to the FE model of the full ring geometry. The single segment model is curved, and cyclic symmetry was used to take into account the ring stiffness of the structure and simulate neighbouring segments. The only boundary condition that was used is a fixed support at the bottom of MP flange (see Chapter 4.1 for more on this model).

#### 6.1.1 Model setup

For model simplification, the bolt was not modelled. Contact surfaces are defined as follows:

- Frictional ( $\mu=x$ ) contact between MP and TP
- Frictional ( $\mu=x$ ) between blocks and MP and TP
- Frictional ( $\mu=x$ ) between blocks and wedges

An automatic mesh is used with 'fine' relevance center, refined at the contact surfaces between shells and MP/TP flanges with mesh size 20 mm (**Error! Reference source not found.**).

The loads are applied in two steps. At the first step the preloading  $F_{\text{actuate}}=x$  [KN] is applied to the inside of the holes both on the outer and inner wedge, pulling them together. See the highlighted in red in **Error! Reference source not found.**. At the second step the external tensile load is applied at the top surface of the TP flange with magnitude equal to  $x$  [MN].

## 6.2 Perfect structure- FE model description

A perfect full-scale geometry has been set up on ANSYS, Workbench with all fasteners included in order to predict at first step the variation of stresses and then calculate the fatigue damage of the structure for the most critical positions. Following the certain characteristics and results of FE- model are described.

### 6.2.1 Geometry

A full ring of the C1 Wedge connection is modelled with the outer diameter of both upper flange (TP) and lower flange (MP) being equal to 7 [m]. Above and below the connection itself, 15 [m] of additional wall has been modelled. The difference with all previous full-ring models is that in this model fastener assembly is installed in every hole around the circumference of the structure. Bolts are not modelled for simplification (**Error! Reference source not found.**).

### 6.2.2 Materials

All components of the C1 Wedge Connection designed as structural steel. A linear material model is selected, with  $E=200$  GPa.

### 6.2.3 Contact

Contact surfaces are defined between the following components. At all previous analysis the friction coefficient used was  $\mu=x$ . Based on calibration tests' results was proved that this friction coefficient is too conservative [13], resulting in less contact force from preload at MP/TP interface. Hence, a more realistic value is used at the following analysis. The type of contact and friction coefficient are presented in Table 9.

Table 9- Contact surface definition FE model.

Contact	Target	Type	$\mu$
Upper flange( <b>perfect</b> )	Lower flange( <b>imperfect</b> )	Frictional	
Upper block	MP/TP flange	Frictional	

Lower block	MP/TP flange	Frictional	
Inner/Outer wedges	Upper/Lower shells	Frictional	
Inner wedge	Outer wedge	Frictional	
Inner wedge	MP/TP flange	Frictional	
Outer wedge	MP/TP flange	Frictional	

### 6.2.4 Mesh

Automatic meshing is performed at the whole structure with 'coarse' relevance center and 2000 [mm] goal element size (**Error! Reference source not found.**). At the eight most critical holes of MP, where the stresses are calculated, the components and the inner surfaces of MP holes are meshed with mesh size 10 [mm] and refined extra with refinement depth '3' (**Error! Reference source not found.**)

### 6.2.5 Boundary conditions

A fixed boundary condition is applied to the bottom of the lower flange (MP) which is 15 [m] below the contact surface between MP and TP flanges.

### 6.2.6 Loads

Three load steps are defined:

1. Preloading: apply  $F_{actuate}=x$  [KN] to the inside of the holes both on the outer and inner wedge, pulling them together (Figure 6.1).
2. ULS tension: the actuation load is maintained, while an external bending moment is applied to the top of the upper flange (TP) with magnitude  $x$  [N\*mm], aligned such that the maximum tensile load experienced at the middle of the eight holes which are mentioned in **Error! Reference source not found.**
3. ULS compression: Using the same model and maintained the actuation load, we apply an external moment with the same magnitude as in step 2 but now aligned such that the maximum compression load experienced at the middle of the eight holes.

*Figure 6.1- Applying preload on both inner and outer wedge at all fastener assemblies around the circumference.*

### 6.2.7 Results

At this certain analysis, the preloading forces were applied at once in all fastener assemblies and the external bending moment was divided into 10 sub steps. The maximum principal

stresses for the Lower flange (MP) are taken as result from this model for the 8 holes (4 left and 4 right from the position with the maximum tension & compression respectively. The resulting maximum principal stresses for the two most critical MP holes (No 4 & 5) after application of the maximum bending moment are presented in the figure below (**Error! Reference source not found.**).

As it is clear from the previous contour plot of MP stresses, the maximum value of principal stress is observed at the same position in all holes and specifically at the start of the top curved part (**Error! Reference source not found.**). From the analysis ,the fluctuation of stresses around the node with the maximum stress is found quite large and in order to take more realistic results about the stress fluctuation during the loading phase a mean stress is used taking into account the neighbouring nodes from the node where the peak stress is appeared (**Error! Reference source not found.**). The same method is applied for each of the eight holes of MP flange and the variation of stresses from full compression to full tension are presented in the following graph (**Error! Reference source not found.**).

### 6.3 Imperfect structure

For this certain analysis the selection of the imperfect structure geometry was done according to the previous analysis results on chapter 5.4. It is obvious that the worst scenario regarding the gap closing behaviour is appeared on the structure with the imperfect segment only at the lower flange MP. In that case the gap stays open with larger magnitude compared to the other two cases. Following this, the imperfect structure includes an imperfect part 30 degrees with 1.5 [mm] gap height only at MP flange and perfect upper flange (TP). The loads and mesh kept the same as for the perfect structure and the stress variations for the same eight holes are presented below (**Error! Reference source not found.**).

### 6.4 Stress Concentration Factor calculation for both perfect and imperfect structure

At the following graph (**Error! Reference source not found.**) the Stress Concentration Factor (SCF) versus the nominal stress at TP flange is plotted for the first four holes of perfect and imperfect structure as calculated numerically. The rest four holes are not presented due to symmetry. As SCF it is called the ratio between the  $\Delta\sigma$  principal at lower flange MP and  $\Delta\sigma$  nominal at upper flange TP (Equation 13). From the graph can be stated that the fatigue damage for perfect structure is similar for all holes which is also proved by the results on Table 11 based on analytical calculations. Regarding the imperfect structure, from the graph is clear that the SCF is higher for holes 2 and 3. Therefore we expect the higher fatigue damage in these holes. Based on specific load spectrum, during lifetime of the structure most of the nominal stress ranges are around zero thus the higher fatigue damage is computed for the hole 3 & 6. This is proved after analytical calculations; which results are presented on Table 12.

$$SCF[-] = \frac{\Delta\sigma(\text{principal})_{MP}}{\Delta\sigma(\text{no min al})_{TP}}$$

Equation 13- Stress concentration factor definition

## 6.5 Fatigue damage calculation according to DNVGL-RP-C203 based on peak stress

At this chapter the fatigue damage for the perfect & imperfect structure is calculated. For this analysis as input is used a realistic load spectrum for a wind turbine with dimensions described in Chapter 1.6 (Figure 6.2).

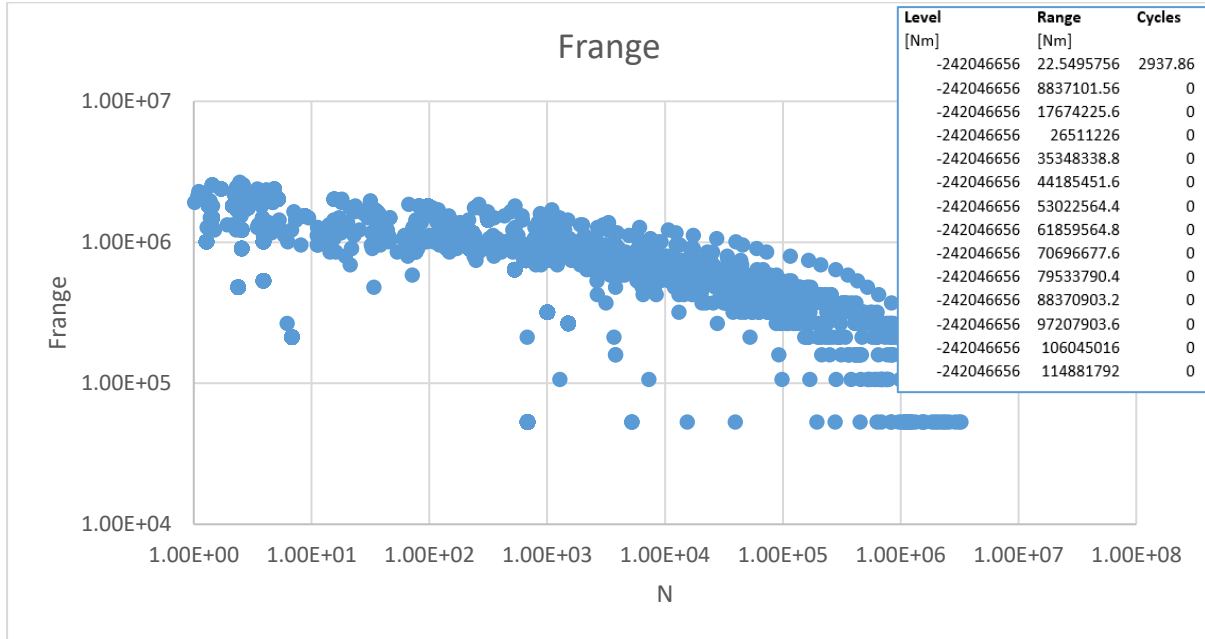


Figure 6.2- Load spectrum used for the fatigue analysis of perfect & imperfect structure with an identical part of the table.

The procedure with all analytical calculations is presented step by step below:

1. Resulting maximum & minimum axial load per segment using the load spectrum input.

$$F_{seg.mean} = \frac{M_{mean} \times A_{seg}}{W} \quad F_{seg.range} = \frac{M_{range} \times A_{seg}}{W}$$

Using these formulas, we calculate the maximum and the minimum axial force per segment:

$$F_{seg.max} = F_{seg.mean} + 0.5 \times F_{seg.range}$$

$$F_{seg.min} = F_{seg.mean} - 0.5 \times F_{seg.range}$$

2. Maximum & minimum stress per segment.

$$\sigma_{nom(max)} = \frac{F_{seg.max}}{A_{seg} \times t_{MP}} \qquad \sigma_{nom(min)} = \frac{F_{seg.min}}{A_{seg} \times t_{MP}}$$

3. In order to calculate the  $\sigma_{max}$  and  $\sigma_{min}$  for each hole of MP flange, the stress curve equation is needed. Thus, a transfer function is used with bi-linear and tri-linear approximation to simulate the actual stress curve taken by FE analysis. Characteristic examples of this method are presented below (**Error! Reference source not found.**, **Error! Reference source not found.**). Then the stress range  $\Delta\sigma$  is calculated.

$$\text{Stress range } (\Delta\sigma) = \sigma_{max} - \sigma_{min}$$

4. According to DNVGL-RP-C203 (chapter 2.5) before entering the S-N curve the calculated stress range calculated at previous step, may be multiplied by the reduction factor  $f_m$ . This is valid in our case as long as the base material not significantly affected by residual stresses due to welding. Consequently, the stress range should be reduced if part of the stress cycle is in compression. The reduction factor  $f_m$  is derived from the following equation:

$$f_m = \frac{\sigma_t + 0.6|\sigma_c|}{\sigma_t + |\sigma_c|} \quad [8]$$

where

$\sigma_t$  = maximum tension stress where tension is defined as positive

$\sigma_c$  = maximum compression stress where compression is defined as negative

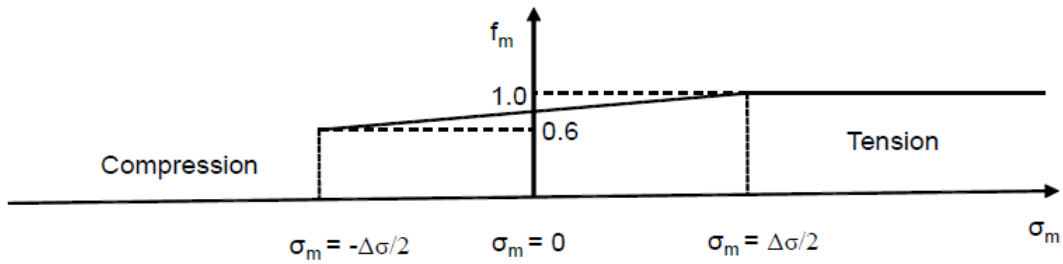


Figure 6.3- Stress range reduction factor to be used with the S-N curve for base material [8].

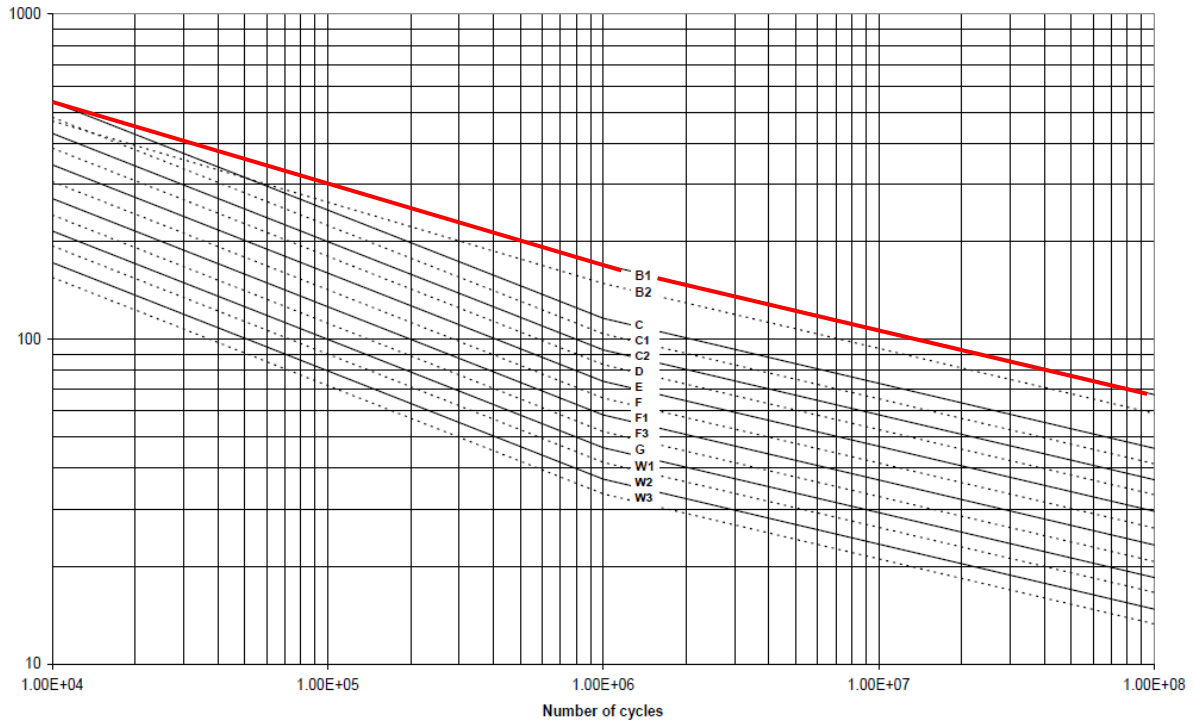


Figure 6.4- S-N curves in air.[8]

Table 10- S-N curves in air.[8]

S-N curve	$N \leq 10^6$ cycles		$N > 10^6$ cycles $\log \bar{a}_2$ $m_2 = 5.0$	Fatigue limit at $10^7$ cycles (MPa) *)	Thickness exponent $k$	Structural stress concentration embedded in the detail (S-N class), see also equation (2.3.2)
	$m_1$	$\log \bar{a}_1$				
B1	4.0	14.917	17.146	106.97	0	
B2	4.0	14.685	16.856	93.59	0	
C	3.0	12.192	16.320	73.10	0.05	
C1	3.0	12.049	16.081	65.50	0.10	
C2	3.0	11.901	15.835	58.48	0.15	
D	3.0	11.764	15.606	52.63	0.20	1.00
E	3.0	11.610	15.350	46.78	0.20	1.13
F	3.0	11.455	15.091	41.52	0.25	1.27
F1	3.0	11.299	14.832	36.84	0.25	1.43
F3	3.0	11.146	14.576	32.75	0.25	1.61
G	3.0	10.998	14.330	29.24	0.25	1.80
W1	3.0	10.861	14.101	26.32	0.25	2.00
W2	3.0	10.707	13.845	23.39	0.25	2.25
W3	3.0	10.570	13.617	21.05	0.25	2.50

\*) see also [2.11]

5. Using S-N curve B1 with characteristics indicated with red at the previous Table 10, the number of cycles to failure are calculated for each stress range and for every hole using the formula:

$$\log(N) = \log(a) - m \log(\Delta\sigma)$$

6. The total fatigue damage is calculated based on the S-N fatigue approach under the assumption of linear cumulative damage (Palmgren-Miner rule) [8]. The fatigue criterion reads:

$$D = \sum_{i=1}^k \frac{n_i}{N_i} \leq 1$$

where

D = accumulated fatigue damage

$n_i$  = number of stress cycles in stress block i

$N_i$  = number of cycles to failure at constant stress range  $\Delta\sigma_i$

k = number of stress blocks

The total fatigue damage for every hole of perfect and imperfect structure is presented at the following tables.

Table 11- Fatigue damage for perfect structure.

Hole	1	2	3	4	5	6	7	8
Damage(%)								

Table 12- Fatigue damage for imperfect structure.

Hole	1	2	3	4	5	6	7	8
Damage(%)								

## 6.6 Fatigue assessment of imperfect structure based on nominal stress

### 6.6.1 Description of method

A different method is used for fatigue damage calculation of the same imperfect structure as described in Chapter 6.3. Contrary to the previous fatigue analysis based on peak stress of MP nodes, this method is based on nominal stress ranges at the lower flange MP, below the eight holes of imperfect segment. In order to read out the stress results on this position, the surface of imperfect segment is divided in eight evenly segments as it is presented in **Error! Reference source not found.**

### 6.6.2 Nominal stress curves extracted from FE analysis

The nominal stress under each MP hole versus the nominal stress at TP from ULS compression to ULS tension is plotted at the following graph (**Error! Reference source not found.**).

From the comparison between the previous graph and the graph based on peak stress for the imperfect structure (**Error! Reference source not found.**), it is clear that the stress ranges based on nominal stress are more linear. This can be explained from the position of the areas where the stresses are extracted and the load path during preload and external loading phase.

### 6.6.3 Nominal stress ratio of imperfect structure

At the following graph the Nominal stress ratio versus the nominal stress at TP flange is plotted from ULS compression to ULS tension and the results for the eight holes of the imperfect segment are presented below (**Error! Reference source not found.**). As nominal stress ratio is called the ratio between  $\Delta\sigma$  nominal at MP below the MP holes and  $\Delta\sigma$  nominal at TP (Equation 14). Actually, this factor represents how is the magnitude of the force carried by every hole of the imperfect MP segment due to external load on TP shell. The factor is higher for holes 2 & 7, and thus are the positions where we expect higher fatigue damage.

$$Nominal\_stress\_ratio[-] = \frac{\Delta\sigma(nominal)_{MP}}{\Delta\sigma(nominal)_{TP}}$$

*Equation 14- Nominal stress ratio definition.*

### 6.6.4 Fatigue damage calculation

For the fatigue damage calculation the same method according to DNVGL-RP-C203 [8] is followed as described in Chapter 6.5. In that case, a different S-N is used based on fatigue test experiments taken place at TU Delft laboratory (**Error! Reference source not found.**) [13]. The parameters of this curve are  $m=x$  and  $\log a=x$ . Using linear cumulative damage, the total fatigue damage for every hole of imperfect segment is calculated and presented on Table 13.

Table 13- Fatigue damage of imperfect structure based on nominal stress.

Hole	1	2	3	4	5	6	7	8
Damage(%)								

## 7 Conclusions & Recommendations

### 7.1 Conclusions

From all different scenarios that were analyzed regarding the position of the gap among the parts of the connection, it has been concluded that the worst case is the presence of the gap on .....side. In that case, the magnitude of the remaining gap is larger and the contact force at TP/MP interface is smaller.

An interconnected piece regarding the gap closing behavior of the structure is the stiffness of different parts. A method proposed by Seidel for analytical stiffness calculation and adapted to C1 Wedge Connection has good accuracy with respect to numerical method, especially for the MP. The TP stiffness is being overestimated by ~30% which is on the conservative side regarding the gap closing behavior. The maximum closeable gap is approximated analytically being equal to the average and not the sum of the maximum deformation of MP and TP. This can be explained because due to progressive closing of the gap, the stiffness of the combined system is higher.

Regarding now the damage calculation, it is assumed the worst scenario 30° gap length with x [mm] gap height only at MP side. Two different approaches and S-N curves are used for fatigue damage calculation. At the first approach which is based on the peak stress of a node, according to B1 S-N curve from DNVG-RP-C203, it is resulted that the imperfect structure is not able to withstand the damage loads (Table 15). In contrast, the damage ratio in all holes of MP in a perfect structure is lower than the acceptable limit, 1 (Table 14). More specifically, in case of perfect structure, the most critical positions are the holes where the maximum tensile load is applied Hole 4 & 5. The same cannot be stated for imperfect case. The largest fatigue damage is appeared at the holes where the gap is closed after preloading, and later opens again.

Table 14- Fatigue damage for perfect structure based on peak stress.

Hole	1	2	3	4	5	6	7	8
Damage(%)								

Table 15- Fatigue damage for imperfect structure based on peak stress.

Hole	1	2	3	4	5	6	7	8
Damage(%)								

At the second approach, the fatigue damage is calculated according to specific S-N curve of C1 Wedge Connection based on fatigue single segment test results. The stress ranges are calculated at the position exactly below the MP holes in order to avoid such point stress differences. The largest damage is appeared again at the same holes and not in the position with largest absolute stress (Table 16). Compared to the previous method (based on peak stress), the fatigue damage is much less and more realistic based on test results. Additionally,

is more symmetric and less sensitive to mesh details which can have a decisive influence on results.

Table 16- Fatigue damage of imperfect MP based on nominal stress.

Hole	1	2	3	4	5	6	7	8
Damage(%)								

## 7.2 Recommendations

As it has been already been referred, the combined TP stiffness is overestimated by ~30%. This is mainly produced by the assumption that the behavior of transition piece (TP) can be described by a perfect parallel spring system. Even though the assumption is conservative regarding the maximum closeable gap, as it leads in underestimation of TP deformation, in reality the behavior is different.

Additionally, the stiffness of TP flange is calculated analytically as a straight beam with the cross section of TP flange but without holes and based on numerical results the factor  $x$  is added on the denominator. Despite the analytical formulas has a good approximation compared to FEA results, it is only validated for this certain geometry of TP flange and cannot state whether can be used generally. For that reason, it would be noteworthy to search for more information regarding the cross-section properties ( $EI$ ,  $GA_s$ ) to take into account the presence of holes and the curvature of the actual TP-flange geometry.

For the purpose of this thesis regarding all Finite Element models, the preload at the bolts is applied by once along the full circumference. In reality this never happens. Hence, the behavior of an imperfect structure and the gap closing procedure need to be investigated for different preloading order of the bolts, especially on the imperfect segment.

Last, it should be noticed that the experiments that have been done until now, are based on a single segment of the wedge connection. This is not curved as happened with the real one and does not provide/ simulate the whole stiffness of the ring. Thus, performing experiments on a scaled full ring of the connection will help to have better view of the global behavior of the connection under several types of loading. Full ring experiments provide the ability to simulate an imperfect case with presence of a gap.

## 7.3 Industry guidelines

According to DIBt guidelines [14], the maximum allowable flatness deviation per flange is 2.0 [mm] over the entire circumference and maximum 1.0 [mm] per flange over a segment of 30°.

For interpretation of the research results, the characteristics of fatigue assessment for our reference wind turbine structure are listed:

- ULS line load  $x$  [MN/m]
- DEL= $x$  MN/m

- TP wall thickness= $x$  mm
- MP wall thickness= $x$  mm
- Assumed gap only at....
- 30° segment with  $x$  mm gap

It can be stated that the ULS and DEL line load levels are high compared to current wind turbines up to  $x$  MW. Additionally, the imperfect segment has been selected being only at MP side which was proved from the analysis that it constitutes the worst scenario. Furthermore, comparing this gap to DIBt guidelines it is  $x\%$  larger and it is unlikely that both opposite flanges have the same imperfection at the same location. Considering the test validated fatigue resistance, the C1 Wedge Connection can withstand lifetime fatigue when DIBt guidelines on waviness are met. It is recommended that a specific study using the nominal stress method is performed on a case-by-case basis, considering the exact geometry and load spectrum.



## 8 Bibliography

- [1] A.Simone, *An Introduction to the Analysis of Slender Structures*, Delft: TU Delft, 2011.
- [2] S.Timoshenko, "On the correction for shear of the differential equation for transverse vibrations of prismatic bars," *Philosophical Magazine* no. 41, pp. 744-746, 1922.
- [3] S. Timoshenko, "On the transverse vibrations of bars of uniform cross-section," *Philosophical Magazine*, no. 43, pp. 125-131, 1922.
- [4] M. Seidel, "Tolerance requirements for flange connections of wind turbine support structures", 2018.
- [5] L. Damkilde, "Stress and stiffness analysis of beam-sections", November 2000.
- [6] Eurocode 3: Design of steel structures, part 1-9: Fatigue. *European Standards*, May 2005.
- [7] Milan Veljkovic, Marko Pavlovic. Lectures of fatigue, CIE 5126. *Technical University of Delft*, 2017.
- [8] DNVGL-RP-C203. Fatigue design of offshore steel structures. April 2016.
- [9] Ansys. Ansys mechanical structural nonlinearities: Introduction to contact. Customer training material, December 2010.
- [10] Dimitrios Billionis, Dimitrios Vamvatsikos. Probabilistic fatigue life assessment of an offshore wind turbine. *5<sup>th</sup> ECCOMAS Thematic Conference on Computational Methods in Structural Dynamics and Earthquake Engineering*, May 2015.
- [11] Dimitrios Billionis, Dimitrios Vamvatsikos. Fatigue analysis of an offshore wind turbine in Mediterranean Sea under a probabilistic framework. *VI International Conference on Computational Methods in Marine Engineering*, May 2015.
- [12] ANSYS. Ansys Meshing Advance Techniques. April 2017.
- [13] RND-01-STGR0202. Fatigue test - TU Delft scaled 2 – Test report – C4. *C1 Connections BV*
- [14] Mitteilung des BIBt. Richtlinie für Windenergieanlagen. Oktober 2012.



## 9 Appendix A: Solution of Analytical Timoshenko model using MAPLE software

### 9.1 Deriving the governing equations of analytical model

To solve the schematized analytical model from Figure 9.1 the Timoshenko beam theory is applied [2], [3]. To take the deflection at the middle of the beam with fixed ends under distributed load  $q(x)$ , the governing equations will be derived.

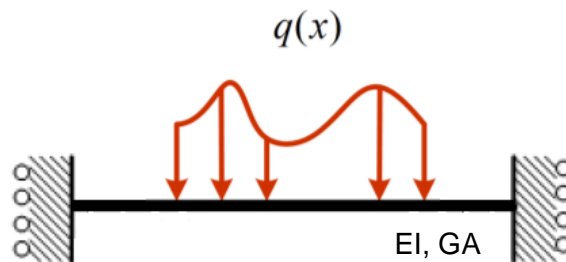


Figure 9.1- Overview of analytical model schematization.

#### **Kinematic equations**

First, the derivation is started by deriving the kinematic equations following the starting assumptions for the Timoshenko theory. That is plane sections remain plain but contrary to the Euler-Bernoulli theory they do not remain perpendicular to the neutral axis [1]. The assumptions for positive directions are shown in Figure 9.2.

$$S_x(x, y) = -\varphi(x) \cdot y$$

$$S_y(x, y) = v(x)$$

$$\varepsilon_{xx} = \frac{dS_x}{dx} = -y \cdot \frac{d\varphi}{dx}$$

$$\gamma_{xy} = \frac{dS_x}{dy} + \frac{dS_y}{dx} = -\varphi + \frac{dv}{dx}$$

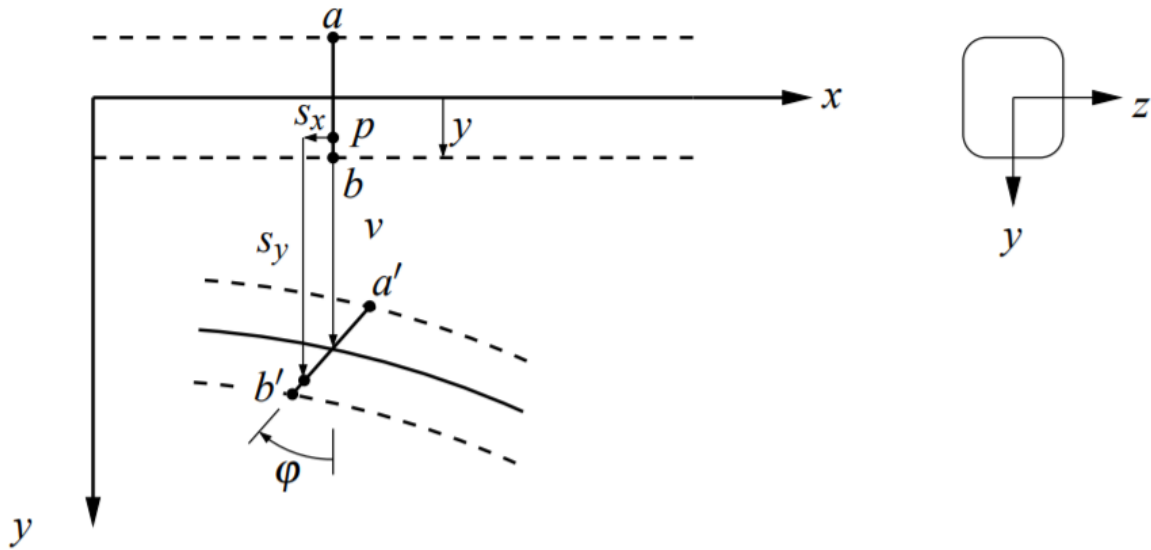


Figure 9.2- Assumed directions for derivation of kinematic equations.

$$\tan(\theta) = \frac{dv}{dx}$$

$$Rd\theta = ds$$

$$\frac{ds}{d\theta} = R$$

$$\frac{1}{R} = k = \frac{d\theta}{ds}$$

We assume that the rotations of the beam stay small. Therefore, the following approximation holds:

$$\sin(\theta) \approx \tan(\theta) \approx \theta$$

$$ds \approx dx$$

And thus:

$$k = \frac{d\theta}{dx}$$

$$\theta = \frac{dv}{dx}$$

$$k = \frac{d^2v}{dx^2}$$

This solves the kinematic equations for the Timoshenko theory.

**Equilibrium equations**

What follows is the equations that relate to the force equilibrium of the model. The positive force directions are indicated in Figure 9.3. This figure shows an infinitesimal segment of the beam for which the equilibrium conditions must hold. For this model second order terms of derivatives are neglected [2].

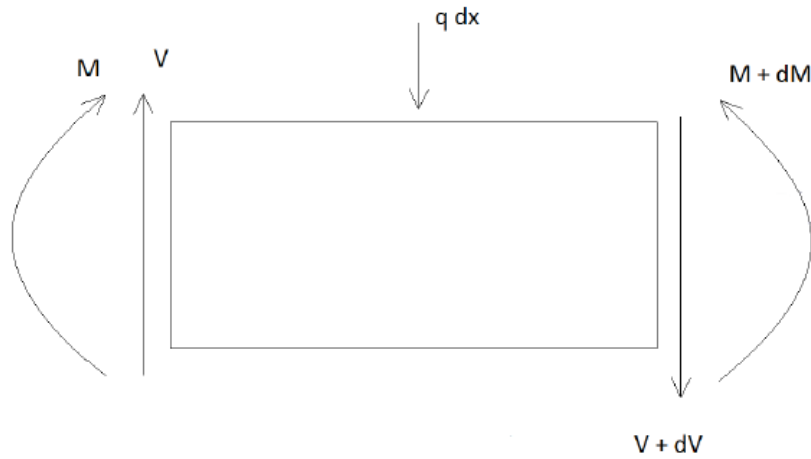


Figure 9.3- Positive force directions equilibrium equations.

Now we can derive the equilibrium conditions of the model:

$$\Sigma M = 0$$

$$\Sigma M = M + dM - M - V \cdot dx = 0$$

$$\Sigma M = dM - V \cdot dx = 0$$

$$dM = V \cdot dx$$

$$\frac{dM}{dx} = V$$

$$\Sigma F_y = 0$$

$$\Sigma F_y = V + dV - V + q \cdot dx = 0$$

$$dV + q dx = 0$$

$$\frac{dV}{dx} + q = 0$$

$$\frac{dV}{dx} = -q$$

### Constitutive equations

Last to complete the derivations of the governing equations is the constitutive equations. These relate the displacements and deformations to the stresses that occur in the material [2]. Hereby  $E$  is the young's modulus of the material,  $G$  the shear modulus,  $A_s$  the effective area in shear and  $I$  the second moment of inertia of the cross-section.

$$\begin{aligned}
 dM &= \sigma_x \cdot y \cdot dA \\
 \int dM &= M = \int \sigma_x \cdot y \cdot dA \\
 \int \sigma_x \cdot y \cdot dA &= \int E \cdot \varepsilon_{xx} \cdot y \cdot dA \\
 \int E \cdot \varepsilon_{xx} \cdot y \cdot dA &= -\int E \cdot y \cdot \frac{d\varphi}{dx} \cdot y \cdot dA \\
 -\int E \cdot y \cdot \frac{d\varphi}{dx} \cdot y \cdot dA &= -E \cdot \frac{d\varphi}{dx} \cdot \int y^2 \cdot dA = -E \cdot I \cdot \frac{d\varphi}{dx}
 \end{aligned}$$

Again, making use of the assumption of small rotations we can find the following:

$$\gamma = \tan \frac{dv}{dx} \approx \frac{dv}{dx}$$

$$\tau = G \cdot \gamma$$

$$\tau = \frac{V}{A_s}$$

$$\gamma = \frac{V}{G \cdot A_s}$$

$$\gamma = -\varphi + \frac{dv}{dx}$$

$$V = GA_s \left( \frac{dv}{dx} - \varphi \right)$$

Combining all the above equations we can find the governing equations for the specific problem:

$$\begin{aligned}
 \frac{dM}{dx} &= V = -EI \cdot \frac{d^2\varphi}{dx^2} \\
 -EI \cdot \frac{d^2\varphi}{dx^2} &= GA_s \cdot \left( \frac{dv}{dx} - \varphi \right)
 \end{aligned}$$

$$V = GA_s \left( \frac{dv}{dx} - \varphi \right)$$

$$\frac{dV}{dx} = GA_s \cdot \left( \frac{d^2v}{dx^2} - \frac{d\varphi}{dx} \right) = -q$$

So, to summarize we find two second order coupled differential equations which govern the deflection of the TP -flange loaded by the preload forces which act as a distributed load along the full length of the beam.

$$GA_s \cdot \left( \frac{d^2v}{dx^2} - \frac{d\varphi}{dx} \right) = -q$$

$$GA_s \cdot \left( \frac{dv}{dx} - \varphi \right) + EI \cdot \frac{d^2\varphi}{dx^2} = 0$$

The equations above govern the deflection of the analytical model. To formulate a solution to these equations the boundary conditions must be considered. The boundary conditions are summarizing below in Table 17. An overview of the solution fields is also given in Figure 9.4.

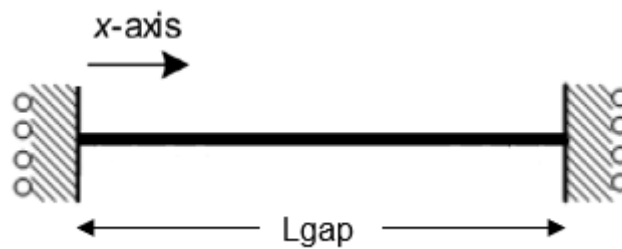


Figure 9.4- Analytical model with solution field.

Table 17- Overview of boundary conditions analytical model.

Left boundary (x=0)	Right boundary (x=L)
V=0	V=0
Φ=0	Φ=0

## 9.2 Solving the governing differential equations

To solve the two coupled differential equations derived above using the boundary conditions from Table 17, MAPLE software is used and the full script used to determine the deflection of the TP-flange at the middle ( $x=L/2$ ) is presented below.

```

> restart;
> DV1 := EI·diff(phi(x), x$2) + GA·(diff(w(x), x) - phi(x)) = 0;
      DV1 := EI  $\left(\frac{d^2}{dx^2} \phi(x)\right) + GA \left(\frac{d}{dx} w(x) - \phi(x)\right) = 0$  (1)
> DV2 := GA·(diff(w(x), x$2) - diff(phi(x), x)) = -q;
      DV2 := GA  $\left(\frac{d^2}{dx^2} w(x) - \frac{d}{dx} \phi(x)\right) = -q$  (2)
> sol1 := dsolve({DV1, DV2}, {w(x), phi(x)}): assign(sol1):
> w := (w(x)): phi := (phi(x)):
> Gam := diff(w, x) + phi: kappa = diff(phi, x):
> alpha_bending := phi: alpha_shear := diff(w, x):
> V := GA·Gam: M = EI·kappa:
> x := 0: eq1 := w = 0: eq2 := phi = 0:
> x := L: eq3 := w = 0: eq4 := phi = 0:
> sol2 := solve({eq1, eq2, eq3, eq4}, {_C1, _C2, _C3, _C4}): assign(sol2): x := 'x':
      sol2 :=  $\left\{-C1 = -\frac{qL}{2EI}, -C2 = -\frac{q(-GAL^2 + 12EI)}{12EIGA}, -C3 = \frac{qL}{2GA}, -C4 = 0\right\}$  (3)
>
> x :=  $\frac{L}{2}$ : simplify(w);
      
$$\frac{qL^2(GAL^2 + 48EI)}{384EIGA}$$
 (4)

```

## 10 Appendix B: Input data for ANSYS

In chapter 2 in Finite Element Analysis, structural steel with the following characteristics was used.

### 10.1 Steel

Table 18: Density and Elastic for structural steel.

Density:	7850 Kg/m <sup>3</sup>
Elastic:	
Young's modulus	Poisson's ratio
200000 MPa	0.3
Shear modulus	
76923 MPa	

## 11 Appendix C: Input data for analytical calculations

In order to calculate analytically the linear stiffness of TP flange, the second moment of inertia (I) and the Shear Area ( $A_{eff}$ ) are needed.

### 11.1 Second moment of Inertia

The second moment of Inertia of the full cross section without holes is used and calculated equal to  $I_{xx}$  [mm<sup>4</sup>] using Solid Edge 2019 software (Figure 11.1).

## 11.2 Shear Area Aeff

The cross section of TP flange is divided in two areas 1 & 2 (**Error! Reference source not found.**). The Area 1 can be assumed as rectangular cross section and then the effective area

for shear is equal to  $A_{eff1} = \frac{5}{6} \times A_1$  [5].

The Area 2 can be assumed as U-profile and the shear area can be estimated as

$$A_{eff2} = \dots \text{ [mm}^2\text{] [5].}$$

Then the total effective area for shear is  $A_{eff}^{tot} = A_{eff1} + A_{eff2}$  [mm<sup>2</sup>].